


Reservoir Computing with Spin Waves in a Skyrmion Crystal

Mu-Kun Lee* and Masahito Mochizuki

Department of Applied Physics, Waseda University, Okubo, Shinjuku-ku, Tokyo 169-8555, Japan

 (Received 16 February 2022; revised 27 June 2022; accepted 8 July 2022; published 29 July 2022; corrected 16 August 2022)

Magnetic skyrmions are nanometric spin textures characterized by a quantized topological invariant in magnets and often emerge in a crystallized form called a skyrmion crystal in an external magnetic field. We propose that magnets hosting a skyrmion crystal possess high potential for application to reservoir computing, which is one of the most successful information processing techniques inspired by functions of the human brain. Our skyrmion-based reservoir exploits precession dynamics of magnetizations, i.e., spin waves, propagating in the skyrmion crystal. Because of complex interferences and slow relaxations of the spin-wave dynamics, the skyrmion spin-wave reservoir attains several important characteristics required for reservoir computing, e.g., the generalization ability, nonlinearity, and short-term memory. We investigate these properties by imposing three standard tasks to test the performance of the reservoir, i.e., the duration-estimation task, short-term memory task, and parity-check task. Through these investigations, we demonstrate that magnetic skyrmion crystals are promising materials for spintronics reservoir devices. Because magnetic skyrmions emerge spontaneously in magnets via a self-organization process under application of a static magnetic field, the proposed skyrmion reservoir requires neither advanced nanofabrication nor complicated manufacturing for production, in contrast to other previously proposed magnetic reservoirs constructed with fabricated spintronics devices. Our proposal is expected to realize a breakthrough in the research of spintronics reservoirs of high performance.

DOI: [10.1103/PhysRevApplied.18.014074](https://doi.org/10.1103/PhysRevApplied.18.014074)

I. INTRODUCTION

Reservoir computing [1–3] is one of the most successful information processing techniques inspired by the nerve system of the human brain, which is composed of three sectors, i.e., input layer, reservoir, and output layer [see Fig. 1(a)]. Sequential information data are entered via the input layer composed of one or more input nodes. The input signals are transformed to different signals in a nonlinear way through recursively propagating in a dynamical medium called a reservoir. Through this nonlinear transformation, the input data are mapped onto a higher-dimensional information space. Reservoirs are composed of many ingredients connected mutually via physical interactions [1,2] to achieve the nonlinear transformation and are used as a black box in computing because the connections among the ingredients are complicated and usually unknown. The transformed signals are measured at installed readout devices and are subsequently translated to outputs via a linear transformation with a weight vector \mathbf{W}_{out} . The weight vector \mathbf{W}_{out} connects the readout nodes and the output node, which is optimized by training so as to provide correct answers or desired outputs for a given problem. In reservoir computing, we only need to train the weight vector \mathbf{W}_{out} , in contrast to another

established brain-inspired information processing technique called neural network computing [4,5], in which all the weight matrices \mathbf{W}_{res} connecting nodes in the multiple layers must be optimized.

A lot of physical reservoirs have been proposed and demonstrated to date, which are based on, e.g., optical [6–9], mechanical [10–13], biological [14–17], electronic [18–21], and magnetic systems [22–32]. Among them, magnetic reservoirs have attracted a great deal of research interest because they have numerous advantages over other physical reservoirs. The advantages of magnetic reservoirs are (1) nonvolatility [33], (2) durability against environmental agitations [34,35], e.g., radiation, heat, and mechanical shocks, (3) low energy consumption [36], and (4) quick responses [23]. The former two advantages are pronounced in comparison with reservoirs based on optical systems and semiconductors, while the latter two advantages are pronounced in comparison with mechanical reservoirs.

Most of the previously proposed magnetic reservoirs are based on series-connected spin-torque oscillators [22–26]. A spin-torque oscillator is a micrometric or even nanometric sized spintronics device that has a layered nanopillar structure with soft and hard ferromagnetic layers separated by a thin insulating layer. The magnetization in the soft ferromagnetic layer exhibits specific resonant oscillations upon injection of spin-polarized currents or application of

*irlight203@hotmail.com

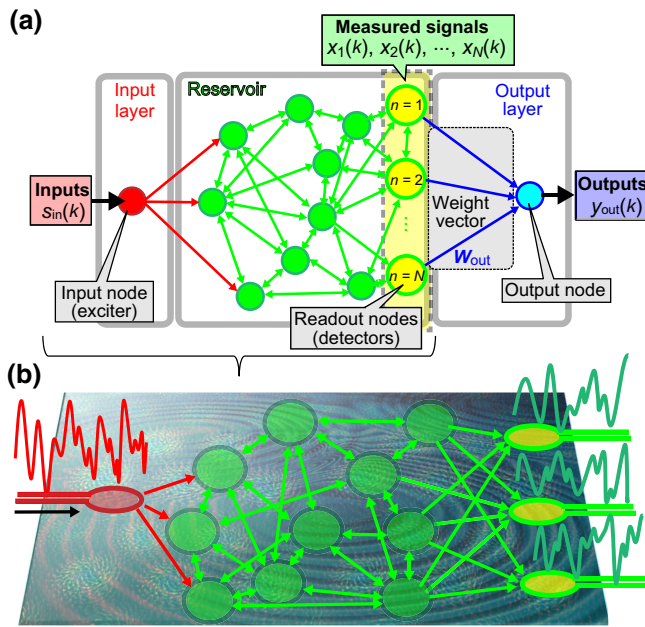


FIG. 1. (a) Architecture of the reservoir computing. The weight vector \mathbf{W}_{out} connecting the reservoir and the output node is required to be optimized by training to produce desired outputs for a given problem. (b) Proposed physical reservoir exploiting spin waves propagating in a thin-plate magnet hosting a magnetic skyrmion crystal. Single or multiple microwave generators are installed near the left edge as input nodes where locally applied microwave fields corresponding to the input data induce magnetization oscillations in the skyrmion crystal. Single or multiple readout nodes called detectors are installed near the right edge that measure local dynamics of magnetizations via an electric voltage induced by the electromagnetic induction. The signals measured at the detectors are translated to outputs via a linear transformation using the optimized weight matrix \mathbf{W}_{out} .

microwaves, while the magnetization in the hard ferromagnetic layer is fixed and hardly changes its orientation. The relative magnetization directions between the soft and hard ferromagnetic layers affect the electric resistance of currents tunneling through the thin insulating layer, and thus the magnetization oscillations in the soft ferromagnetic layer can be detected by the measurement of electric resistance. Spin-torque oscillators in a reservoir interact magnetically via magnetic dipole-dipole interactions or electrically via circuit connections to realize the reservoir functions. Several numerical simulations [23,26] have demonstrated that spin-torque oscillator reservoirs show high performance in information processing. However, it is required to fabricate a number of high-quality spin-torque oscillators of nanometric size with uniform characteristics to realize reservoir functions. Thereby, their production requires advanced nanofabrication techniques, complicated manufacturing processes, and high costs. Under these circumstances, high-performance magnetic reservoirs, which can be produced easily with low costs, are demanded.

Recently, nanometric topological spin textures called skyrmions have attracted a great deal of research interest [37–41]. The concept of a skyrmion was originally proposed in the 1960s as a mathematical model of baryon in particle physics [42,43], which comprises vector fields pointing in all directions wrapping a sphere like a hedgehog. In the 1980s, it was theoretically predicted that skyrmions can emerge in ferromagnets with broken spatial inversion symmetry as a two-dimensional vortexlike spin texture, which can be regarded as a stereo projection of the original hedgehog-type skyrmion onto a plane; see Refs. [44–46], who also predicted that magnetic skyrmions often emerge in a hexagonally crystallized form called a skyrmion crystal. In 2009, magnetic skyrmion crystals were indeed discovered in metallic chiral magnets by small-angle neutron scattering measurements [47] and Lorentz transmission electron microscopies [48]. Skyrmions are characterized by a quantized topological invariant called the skyrmion number representing how many times the magnetizations wrap a sphere [38,49]. This means that magnetic skyrmions belong to a different topological class from ferromagnetic and conical or helical states, and, thereby, we cannot create and annihilate them in a uniform ferromagnetic state by continuous variation of the spatial alignment of magnetizations [49]. Instead, a local reversal of magnetization is required for their creation and annihilation, which necessitates a large energy cost associated with the ferromagnetic exchange interaction. Owing to protection by this energy cost, the magnetic skyrmions are robust against environmental agitations and external stimuli [34].

It was theoretically revealed that a magnetic skyrmion crystal exhibits peculiar spin-wave modes at microwave frequencies, i.e., clockwise and counterclockwise rotation modes active to in-plane microwave fields and a single breathing mode active to out-of-plane microwave fields [50–52]. Magnetic skyrmions constituting a skyrmion crystal uniformly rotate in the two rotation modes, whereas they uniformly expand and shrink in an oscillatory manner in the breathing mode. These modes are similar to the collective modes of a magnetic vortex confined in a magnetic nanodisk or nanopillar [53,54]. In this sense, each skyrmion in a skyrmion crystal can be regarded as a spin-oscillator device carrying the eigenmode spin oscillations. This fact indicates that a magnetic skyrmion crystal and even an assembly of randomly aligned magnetic skyrmions can work as series-connected spin-torque oscillators. It further comes up with an idea of magnetic reservoirs exploiting the spin waves or collective magnetization dynamics of magnetic skyrmions. One advantage of using magnetic skyrmions for reservoirs is that neither advanced nanofabrication techniques nor complicated manufacturing processes are required for production, in contrast to the previously proposed and widely investigated spin-torque oscillator reservoirs because magnetic

skyrmions can be created simply by application of the static magnetic field to a plate-shaped sample of a chiral magnet or magnetic bilayer system [48].

In this paper, we propose a magnetic reservoir device that exploits spin waves or magnetization dynamics propagating in a plate-shaped magnet hosting magnetic skyrmions. We demonstrate that this skyrmion spin-wave reservoir possesses several important characteristics required for reservoir computing, e.g., the generalization ability [27], nonlinearity [23,26], and short-term memory [23,26] owing to their complex interferences and slow relaxations, by imposing three standard tasks to test the performance, i.e., the duration-estimation task, short-term memory task, and parity-check task [23,26]. Through these investigations, we argue that magnetic skyrmions are promising materials for spintronics reservoirs. Because the proposed skyrmion spin-wave reservoir has a lot of advantages over other previously proposed magnetic reservoirs consisting of fabricated spintronics devices, the present work will necessarily mark great progress in the research of reservoir computing.

In realistic systems, thermal fluctuations, disorder, defects, and environmental noises exist. At first glance they might cause negative effects by reducing the robustness of a physical reservoir. However, among the interdisciplinary fields of science, including recurrent neural networks and condensed matter physics, there are intriguingly growing studies revealing the constructive role of noise to the system's performance, such as the noise-assisted recognition and permanence of information or noise-assisted persistence of memory in neural networks [55–58] and, in physical systems, e.g., the noise-enhanced stability of the superconducting state in graphene-based and long Josephson junctions [59–62]. In addition to noises, a rising consensus is also developed showing that a dynamical system may achieve its best performance on machine learning tasks when the model parameters are on the so-called “edge of chaos” in parameter space, which drives the system to locate near the boundary between ordered and chaotic phases, at which the highest nonlinearity manifests itself in the system [63,64]. This suggests that the disorder and defect in the system can potentially enhance the performance. In this work as a preliminary study of the performance of our skyrmion spin-wave reservoir, we neglect the effects of noises, defects, and thermal fluctuations, and study the magnetization dynamics at zero temperature. For the eventually practical applications, these aspects will be the subject of future investigations.

II. CONCEPT AND METHOD

A. Skyrmion spin-wave reservoir

We first discuss the concept of our skyrmion spin-wave reservoir as shown in Fig. 1(b). A key ingredient of this reservoir is a thin-plate specimen of a skyrmion-hosting

magnet. One or more devices called input nodes are fabricated on the left side of the specimen to enter signals as input data. The entered signals are transformed while they propagate in the specimen recursively. Other devices called readout nodes or detectors are fabricated on the right side of the specimen to measure the transformed signals.

The information processing with this skyrmion-based reservoir system is performed as follows. We apply out-of-plane microwave magnetic fields \mathbf{H}^o to enter the input data, which are locally generated by injecting electric currents j_{in} to a metallic ring fabricated as an input node on the specimen. More concretely, a series of input data are entered after being translated to the time-dependent amplitude and duration of the microwave pulses. The applied microwave pulses induce magnetization oscillations in the skyrmions, and the induced oscillations propagate in the specimen as spin waves, which exhibit nonlinear or even chaotic behaviors because of complicated interferences due to the distorted configuration of the hexagonal skyrmion crystal. The magnetization oscillations eventually reach the area of readout nodes (detectors). The magnetization dynamics within an area of each detector are measured as time profiles of induced electric currents via the electromagnetic induction.

This skyrmion spin-wave reservoir has advantages over magnetic reservoirs based on spin-torque oscillators. First, complicated nanofabrication is not required because skyrmions are created spontaneously in magnets by application of a magnetic field [48]. We can prepare a skyrmion crystal or an assembly of skyrmions by simply applying a magnetic field or by attaching a ferromagnet to a thin-plate chiral magnet. The created skyrmions are expected to behave as spin-torque oscillators in a series connection. Second, more intense readout signals can be expected for the skyrmion spin-wave reservoirs because the skyrmions directly interact via magnetic exchange interactions and are thus strongly coupled with each other as compared with the series-connected spin-torque oscillators interacting via weak magnetic dipole-dipole interactions or via indirect electric circuit connections [23,26].

In fact, a concept of the spintronics reservoir using magnetic skyrmions was proposed in Refs. [29–31], which is based on the electric current injections to a skyrmion-hosting metallic magnet, that is, the electric currents are injected as input data, while variations of electric resistance due to skyrmions are measured as readout signals. On the contrary, our skyrmion reservoir is based on the spin-wave propagations in the skyrmion-hosting magnet. We expect that our skyrmion spin-wave reservoir can host remarkable nonlinearity because of complicated interferences of spin waves. A pronounced short-term memory effect can also be expected for our reservoir because of the slow damping of magnetization dynamics. Furthermore, we expect durability of the reservoir system because spin waves do not drive magnetic skyrmions so much and thus

hardly affect their spatial positions [50], which might be of practical importance to achieve stable computations.

B. Reservoir computing

We examine potentials of magnetic skyrmions for application to reservoir computing by investigating several characteristics required for physical reservoirs: (1) the generalization ability [27], (2) the short-term memory [23,26], and (3) the nonlinearity [23,26] in response. In our skyrmion reservoir, these properties are carried by spin waves, i.e., precession dynamics of magnetizations, propagating in a thin-plate magnet hosting skyrmions. In the present study, we deal with magnetic skyrmions packed in a rectangular-shaped thin-plate magnet, which form a distorted hexagonal lattice called a skyrmion crystal. It is known that magnetic skyrmions can also appear in a random form depending on the magnetic field strength or the sample quality. We expect that such a random configuration of skyrmions, which is referred to as a skyrmion fabric in Refs. [29–31], also exhibits similar reservoir functions.

A general procedure of computing with the skyrmion spin-wave reservoir is as follows. We take a set of input data for training, $\{s_{\text{in}}^{\text{train}}(k)\}$ ($k = 1, 2, \dots, L_{\text{train}}$), which can be either Boolean-type binary digits or continuous variables. Each data point is entered to a skyrmion-hosting magnetic sample (reservoir) by an out-of-plane magnetic field pulse to trigger dynamics of magnetizations constituting the skyrmions. The induced magnetization dynamics propagate recursively within the reservoir, and after experiencing significant interferences, they finally reach the readout nodes (detectors). Then, the magnetization dynamics at the N detectors are measured as components of the N -dimensional reservoir state vector $\mathbf{x}(k)$, where

$$\mathbf{x}(k) = \begin{pmatrix} x_1(k) \\ x_2(k) \\ \vdots \\ x_N(k) \end{pmatrix}. \quad (1)$$

The component $x_n(k)$ represents a signal measured at the n th readout node by the k th measurement. The signals measured by the k th measurement are translated to the k th output $y_{\text{out}}(k)$ by a linear transformation using the N -dimensional weight vector \mathbf{W}_{out} as

$$y_{\text{out}}(k) = \mathbf{W}_{\text{out}} \cdot \mathbf{x}(k). \quad (2)$$

The components of \mathbf{W}_{out} are k independent and are optimized so as to output desired or correct values of $y_{\text{out}}(k)$ for a given problem or task. This optimization is called training or learning. More specifically, we optimize the weight vector \mathbf{W}_{out} by minimizing the mean squared error (MSE) between the outputs $y_{\text{out}}(k)$ and values desired or expected to be correct for the problem called targets $y_{\text{target}}(k)$.

Note that this translation is based on a linear transformation, and $y_{\text{out}}(k)$ is given by a linear combination of $x_n(k)$ ($n = 1, 2, \dots, N$), while the nonlinear input-output transformation is thoroughly carried by the reservoir.

The MSE, which is also known as the loss function denoted by L , is given by

$$\begin{aligned} L &= \frac{1}{L_{\text{train}}} \sum_{k=1}^{L_{\text{train}}} [y_{\text{target}}(k) - y_{\text{out}}(k)]^2 \\ &= \frac{1}{L_{\text{train}}} \sum_{k=1}^{L_{\text{train}}} [y_{\text{target}}(k) - \mathbf{W}_{\text{out}} \cdot \mathbf{x}(k)]^2. \end{aligned} \quad (3)$$

The optimized weight vector $\mathbf{W}_{\text{out}}^{\text{opt}}$ that minimizes the MSE can be obtained using the pseudoinverse-matrix method [65,66] as

$$\mathbf{W}_{\text{out}}^{\text{opt}} = \mathbf{Y}_{\text{target}}^T \hat{\mathbf{X}}^+. \quad (4)$$

Here $\mathbf{Y}_{\text{target}}$ is the L_{train} -dimensional vector composed of $y_{\text{target}}(k)$, and $\hat{\mathbf{X}}^+$ is the $L_{\text{train}} \times N$ pseudoinverse matrix of the $N \times L_{\text{train}}$ matrix $\hat{\mathbf{X}}$ composed of vectors $\mathbf{x}_n(k)$ [65,66]. They are respectively given by

$$\mathbf{Y}_{\text{target}} = \begin{pmatrix} y_{\text{target}}(1) \\ y_{\text{target}}(2) \\ \vdots \\ y_{\text{target}}(L_{\text{train}}) \end{pmatrix}, \quad (5)$$

$$\hat{\mathbf{X}} = \begin{pmatrix} x_1(1) & x_1(2) & \cdots & x_1(L_{\text{train}}) \\ x_2(1) & x_2(2) & \cdots & x_2(L_{\text{train}}) \\ \vdots & \vdots & \cdots & \vdots \\ x_N(1) & x_N(2) & \cdots & x_N(L_{\text{train}}) \end{pmatrix}. \quad (6)$$

After the optimization of \mathbf{W}_{out} by sufficient training, we input another set of data called testing data $\{s_{\text{in}}^{\text{test}}(\ell)\}$ ($\ell = 1, 2, \dots, L_{\text{test}}$) into the skyrmion spin-wave reservoir. We again measure induced response signals at N readout nodes and construct the N -dimensional reservoir state vector $\mathbf{x}(\ell)$ for the ℓ th measurement. We then translate it to the output $y_{\text{out}}(\ell)$ using the optimized weight vector $\mathbf{W}_{\text{out}}^{\text{opt}}$ and compare thus obtained outputs $y_{\text{out}}(\ell)$ with targets $y_{\text{target}}(\ell)$ to check whether the reservoir can provide correct answers and/or desired outputs.

To investigate three of the required properties of the reservoir, i.e., the generalization ability, short-term memory function, and nonlinearity, we impose the duration-estimation task, short-term memory task, and parity-check task on our skyrmion spin-wave reservoir, respectively. For each task, we choose appropriate magnetic field pulses to represent the input data $\{s_{\text{in}}^{\text{train}}(k)\}$ and $\{s_{\text{in}}^{\text{test}}(\ell)\}$. We also properly define the reservoir state vectors $\mathbf{x}(k)$ and the targets $y_{\text{target}}(k)$ as argued in the following sections.

C. Skyrmion crystal

To describe a skyrmion crystal in the skyrmion spin-wave reservoir, we employ a classical Heisenberg model on a square lattice. The Hamiltonian contains the nearest-neighbor ferromagnetic exchange interactions, Zeeman interactions, and Dzyaloshinskii-Moriya interactions (DMI) as

$$\mathcal{H} = -J \sum_{\langle i,j \rangle} \mathbf{m}_i \cdot \mathbf{m}_j - \sum_i [\mathbf{H} + \mathbf{H}^\omega(\mathbf{r}_i, t)] \cdot \mathbf{m}_i + D \sum_i (\mathbf{m}_i \times \mathbf{m}_{i+\hat{x}} \cdot \hat{x} + \mathbf{m}_i \times \mathbf{m}_{i+\hat{y}} \cdot \hat{y}), \quad (7)$$

where \mathbf{m}_i is a classical magnetization vector at site i , the length of which is normalized to be unity ($|\mathbf{m}_i| = 1$). For the Zeeman-interaction term, we consider two kinds of magnetic fields, i.e., a dc magnetic field \mathbf{H} and a time-dependent ac magnetic field $\mathbf{H}^\omega(\mathbf{r}_i, t)$,

$$\mathbf{H} = H_z \hat{\mathbf{z}}, \quad \mathbf{H}^\omega(\mathbf{r}_i, t) = H^\omega(\mathbf{r}_i) \sin(\omega t) \hat{\mathbf{z}}. \quad (8)$$

The dc magnetic field \mathbf{H} is applied globally to the entire system constantly, whereas the ac magnetic field $\mathbf{H}^\omega(\mathbf{r}_i, t)$ is applied locally to a restricted area regarded as an input node (exciter). For a practical device of the input node, we assume, for example, a micrometric metallic ring to generate a time-dependent local magnetic field within the ring by injecting a temporally varying electric current [see Fig. 1(b)]. Both \mathbf{H} and $\mathbf{H}^\omega(\mathbf{r}_i, t)$ fields are applied perpendicular to the thin-plate plane of the skyrmion-hosting magnet.

The position vector $\mathbf{r}_i = (i_x, i_y)$ represents the integer coordinates of site i in units of the lattice constant. We take $J (\equiv 1)$ as energy units and choose $D = 0.36$ for the strength of DMI. According to the saddle-point equation of the total energy, this DMI parameter leads to a skyrmion diameter of $2\pi / [\tan^{-1}(D/\sqrt{2}J)] \sim 25$ in units of the lattice constant. In the following calculations, the strength of the dc magnetic field is fixed at $H_z = 0.06$, while the amplitude and frequency of the ac magnetic field are fixed at $H^\omega(\mathbf{r}) = 0.008$ and $\omega = 0.12416$, respectively. Note that this dc magnetic field leads to a stable skyrmion crystal in the ground state, while this ac magnetic field efficiently excites a spin-wave mode of the skyrmion crystal called the breathing mode when $D = 0.36$, which are deduced from numerical calculation results for $D = 0.09$ in Ref. [50] after the following scale transformations with $a = 4$ [67]:

$$D \rightarrow aD \implies |\mathbf{H}| \rightarrow a^2|\mathbf{H}|, \quad \omega \rightarrow a^2\omega. \quad (9)$$

The unit conversions from natural units to SI units are summarized in Table I, where $\gamma \equiv g\mu_B/\hbar$ is the gyromagnetic ratio.

TABLE I. Unit conversion table when $J = 1$ meV.

	Dimensionless quantity	Corresponding value with units
Exchange int.	$J = 1$	1 meV
Time	$t = 1000$	$10^3 \times \hbar/J = 0.66$ ns
Frequency	$\omega = 0.01$	$10^{-2} \times J/2\pi\hbar = 2.41$ GHz
Magnetic field	$H = 0.001$	$10^{-3} \times J/\hbar\gamma = 8.64$ mT

The magnetization dynamics induced by applied ac magnetic fields are simulated by numerically solving the Landau-Lifshitz-Gilbert (LLG) equation at zero temperature using the fourth-order Runge-Kutta method [68]. The equation is given by

$$\frac{d\mathbf{m}_i}{dt} = -\frac{1}{1 + \alpha_G^2} [\mathbf{m}_i \times \mathbf{H}_i^{\text{eff}} + \alpha_G \mathbf{m}_i \times (\mathbf{m}_i \times \mathbf{H}_i^{\text{eff}})], \quad (10)$$

where $\alpha_G (= 0.1)$ is the dimensionless Gilbert-damping constant. The effective local magnetic fields $\mathbf{H}_i^{\text{eff}}$ acting on the magnetization \mathbf{m}_i are calculated by the \mathbf{m}_i derivative of the Hamiltonian as

$$\mathbf{H}_i^{\text{eff}} = -\frac{\partial \mathcal{H}}{\partial \mathbf{m}_i}. \quad (11)$$

First, we prepare an initial magnetization configuration in the absence of an ac magnetic field $\mathbf{H}^\omega(\mathbf{r}_i, t)$ by setting $H^\omega(\mathbf{r}_i) = 0$ in the Hamiltonian \mathcal{H} . Figure 2(a) presents the magnetization configuration of a distorted skyrmion crystal confined in a rectangular-shaped square-lattice system of 128×64 sites with open boundary conditions. This magnetization configuration is obtained by Monte Carlo thermalization with simulated annealing to low temperatures, followed by a further relaxation under a sufficient time evolution in the LLG equation. Taking this configuration as an initial state of the reservoir, we apply local ac magnetic fields as inputs for reservoir computing. Specifically, the ac magnetic field $\mathbf{H}^\omega(\mathbf{r}_i, t)$ is applied to a small circular area designed as an input node shown as a red circle in Fig. 2(a). The radius of the circle is 3, and its center is located at $(x, y) = (6.5, 32.5)$, both in units of the lattice constant.

In this work we solve the LLG equation in Eq. (10) at zero temperature [29]. In realistic situations, thermal fluctuations might affect the results. However, in the following tasks we take the out-of-plane magnetization responses averaged over the sites inside detector areas as the components of the reservoir state vector [see Eqs. (13) and (21) below], with the assumption that the isotropic thermal effect averages out in this procedure. [In the generalization ability task, the spatially averaged magnetizations are then averaged over a period of time, as in Eq. (16), which may further reduce the thermal effect.] Meanwhile,

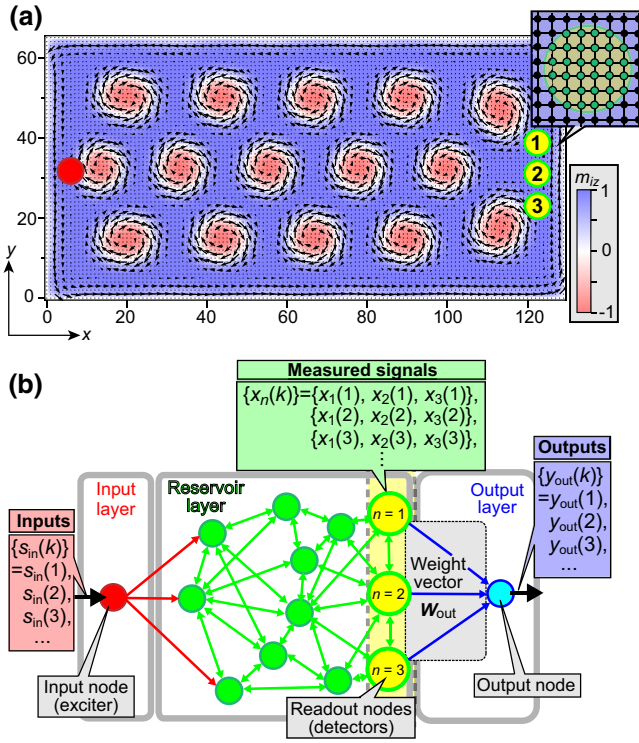


FIG. 2. (a) Magnetization configuration of the skyrmion spin-wave reservoir. Magnetic skyrmions are packed in a rectangular system of 128×64 sites described by the classical Heisenberg model on a square lattice in Eq. (7). In-plane magnetization vectors are presented by arrows at sites (i_x, i_y) when the integer coordinates i_x and i_y satisfy conditions $\text{mod}(i_x, 2) = 1$ and $\text{mod}(i_y, 2) = 1$, while the out-of-plane components are presented by colors. A setup of the input and readout nodes used for the duration-estimation task is also shown. The red circle near the left edge indicates the input area, and three green circles labeled 1, 2, and 3 near the right edge indicate the readout nodes (detectors), each of which has a radius of 3, in units of the lattice constant, and contains 32 sites inside the area. Inset shows a magnified view of a detector. (b) Procedure of the reservoir computing for the duration-estimation task.

finite-temperature skyrmion lattices in thin films have been observed in several works [69,70], which guarantee the stability of the system being considered here at finite temperatures. For future practical applications, thermal fluctuations, environmental noises, and defects must be seriously taken into account to investigate the robustness or even possible enhancement of the performance in our system. Clarifications of these aspects are left to future investigations.

III. RESULTS

A. Duration-estimation task

We first investigate the duration-estimation task. By imposing this task, we examine whether the skyrmion spin-wave reservoir can correctly estimate the durations of input ac magnetic fields as a test for the ability to evaluate

unknown variables of input signals. For this task, various durations $T_{\text{dur},k}$ of the ac magnetic field are chosen as inputs $s_{\text{in}}(k)$ [see also Fig. 2(b)],

$$s_{\text{in}}(k) = T_{\text{dur},k}. \quad (12)$$

We apply a pulse of the ac magnetic field during the time range $0 \leq \bar{t} < T_{\text{dur},k}$ to a small circular area designed as an input node, and, subsequently, turn it off at $\bar{t} = T_{\text{dur},k}$ and let the magnetizations relax. We trace the magnetization dynamics during this process by numerically solving the LLG equation.

The detectors are three circular (green) areas labeled $n = 1, 2$, and 3 in Fig. 2(a). Their radii are 3, in units of the lattice constant, and their centers are located at $(x, y) = (122.5, 40.5)$, $(122.5, 32.5)$, and $(122.5, 24.5)$, respectively. We define t as the time after turning off the ac magnetic field (i.e., $t \equiv \bar{t} - T_{\text{dur},k}$). At each detector, we measure dynamics of local magnetizations. The time profile of z -component magnetization averaged over sites contained in the area of the n th detector is given by

$$M_{z,n}(T_{\text{dur},k}, t) = \frac{1}{N_{\text{detect}}} \sum_{i \in n\text{th detector}} m_{z,i}(T_{\text{dur},k}, t), \quad (13)$$

where $N_{\text{detect}} (= 32)$ is the number of lattice sites within each detector area. We further subtract a steady component $M_{s,n}$ as

$$\Delta M_{z,n}(T_{\text{dur},k}, t) = M_{z,n}(T_{\text{dur},k}, t) - M_{s,n}, \quad (14)$$

where $M_{s,1} = M_{s,3} = 0.9467$ for detectors 1 and 3, and $M_{s,2} = 0.9412$ for detector 2.

Figure 3 shows simulated time profiles of $\Delta M_{z,n}(T_{\text{dur},k}, t)$ for three different ranges of durations $T_{\text{dur},k}$, i.e., (a) shorter durations ($T_{\text{dur},k} = 800\text{--}2000$), (b) intermediate durations ($T_{\text{dur},k} = 2400\text{--}4000$), and (c) longer durations ($T_{\text{dur},k} = 4200\text{--}5800$) at detectors 1, 2, and 3. The plots of $\Delta M_{z,n}(T_{\text{dur},k}, t)$ exhibit temporal oscillations at respective detectors. In these plots, the behaviors of $\Delta M_{z,n}(T_{\text{dur},k}, t)$ show clear dependence on the duration $T_{\text{dur},k}$. We now focus on the plots of $\Delta M_{z,2}(T_{\text{dur},k}, t)$ at detector 2 for intermediate durations in Fig. 3(b2). We find that, as T_{dur} increases, $\Delta M_{z,n}(T_{\text{dur},k}, t)$ monotonically increases in the time range $800 \leq t \leq 1300$ (range A_b), whereas it monotonically decreases in the subsequent time range $1300 \leq t \leq 1750$ (range B_b). We also find that the amplitudes of oscillation monotonically increase for respective durations as time proceeds. Such behaviors are also observed in detectors 1 and 3. These facts indicate that the time profiles of $\Delta M_{z,n}(T_{\text{dur},k}, t)$ ($n = 1, 2$, and 3) involve information about the duration $T_{\text{dur},k}$ of the ac magnetic field.

We adopt nine values of $T_{\text{dur},k}$ in the intermediate duration range, i.e., $T_{\text{dur},k} = 2300 + 200k$ with $k = 0, 1, 2, \dots, 8$ as a set of input data for training. After

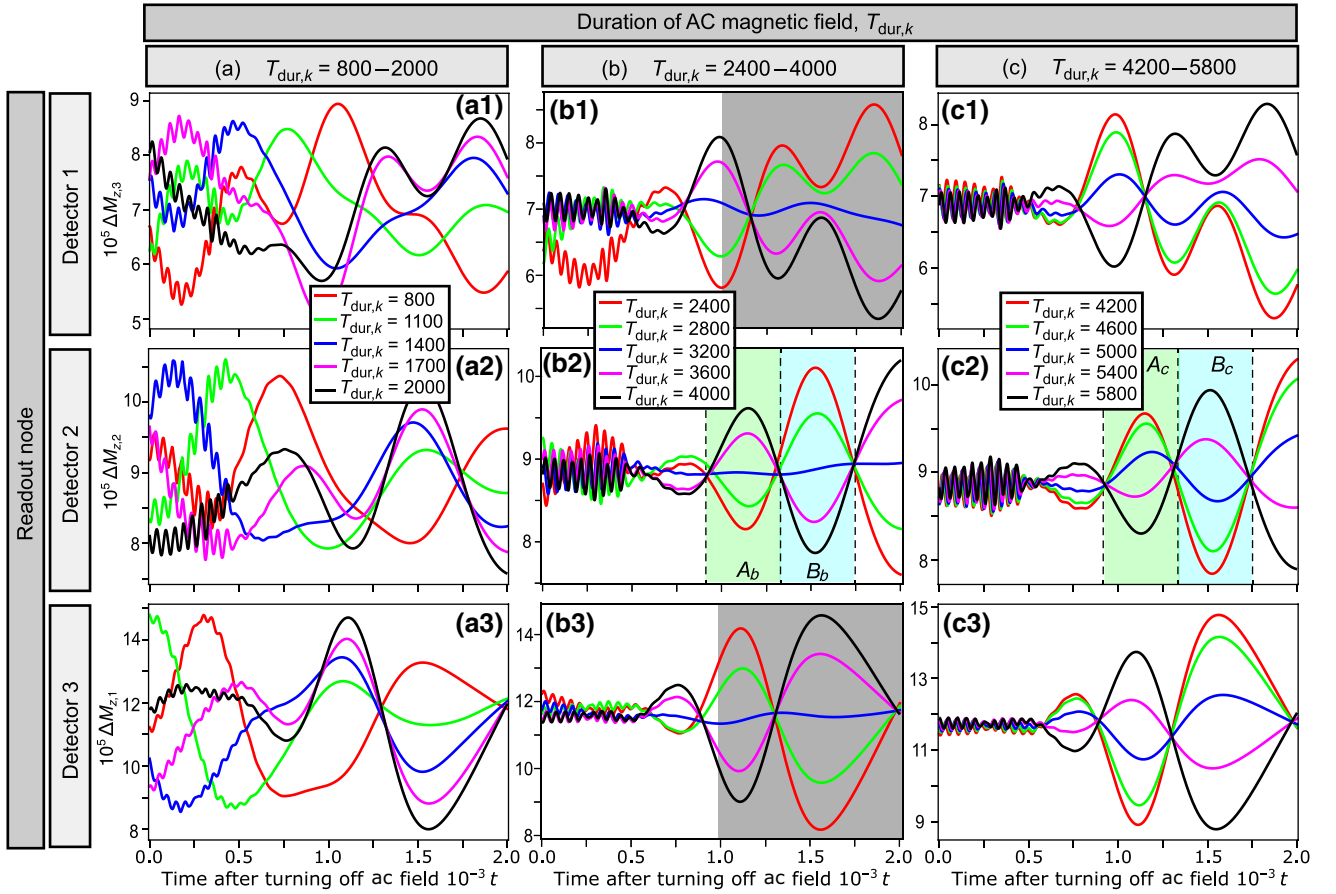


FIG. 3. Selected time profiles of the site-averaged magnetizations $\Delta M_{z,n}(T_{dur,k}, t)$ at each detector after turning off the ac magnetic field with duration $T_{dur,k}$ for various ranges of $T_{dur,k}$, i.e., (a) $T_{dur,k} = 800\text{--}2000$, (b) $T_{dur,k} = 2400\text{--}4000$, and (c) $T_{dur,k} = 4200\text{--}5800$, where t is time after turning off the ac magnetic field. In each duration range, three different detectors labeled $n = 1, 2$, and 3 shown in Fig. 2(a) are examined. We define $\Delta M_{z,n}(T_{dur,k}, t)$ as $\Delta M_{z,n}(T_{dur,k}, t) \equiv M_{z,n}(T_{dur,k}, t) - M_{s,n}$, where $M_{z,n}(T_{dur,k}, t) = \sum_i m_{z,i}(T_{dur,k}, t)/N_{\text{detect}}$ is the out-of-plane component of magnetization averaged over the sites within the area of detector, and $M_{s,n}$ is a steady component. Here $N_{\text{detect}} (= 32)$ is the number of sites within the area of each detector, while the values of $M_{s,n}$ are chosen to be $M_{s,n} = 0.9467$ for detectors 1 and 3, and $M_{s,n} = 0.9412$ for detector 2. Shaded areas in (b1) and (b3) indicate time ranges used to calculate the temporal averages of magnetization in Fig. 4(a) for the duration-estimation task.

applying the ac magnetic field for a certain duration of $T_{dur,k}$, we compute time averages $\langle \Delta M_{z,1}(T_{dur,k}) \rangle_{\text{time}}$ and $\langle \Delta M_{z,3}(T_{dur,k}) \rangle_{\text{time}}$ at detectors 1 and 3 over the time range $1000 \leq t \leq 2000$ indicated by shaded areas in Figs. 3(b1) and 3(b3). We regard these time-averaged magnetizations as reservoir states. Figure 4(a) presents a plot of these quantities as functions of $T_{dur,k}$ for detectors 1 and 3. This plot shows nearly linear behaviors with respect to $T_{dur,k}$ for both detectors, which stem from the monotonic trends of $\Delta M_{z,n}(T_{dur,k}, t)$ with respect to $T_{dur,k}$, as argued above.

Inspired by this characteristic, we devise the following polynomial form with respect to $\langle \Delta M_{z,1}(T_{dur,k}) \rangle_{\text{time}}$ and $\langle \Delta M_{z,3}(T_{dur,k}) \rangle_{\text{time}}$ for output $y_{\text{out}}(k)$:

$$y_{\text{out}}(k) = W_0 + \sum_{m=1}^{m_{\text{max}}} [W_{2m-1} x_1^m(T_{dur,k}) + W_{2m} x_3^m(T_{dur,k})] \quad (15)$$

with

$$x_n(T_{dur,k}) \equiv \langle \Delta M_{z,n}(T_{dur,k}) \rangle_{\text{time}} \times 10^5 \quad (n = 1, 3). \quad (16)$$

Here W_0 is a constant bias, and $m_{\text{max}} (= 3)$ is the maximal power of this polynomial model. The coefficients of linear combination, W_{2m-1} and W_{2m} ($m = 1, 2, \dots, m_{\text{max}}$), are components of the weight vector \mathbf{W}_{out} . In total, there are $2m_{\text{max}} + 1$ components in \mathbf{W}_{out} .

Recalling that the duration-estimation task requires the reservoir to correctly estimate the durations of ac magnetic fields, we set the desired outputs, i.e., the targets $y_{\text{target}}(k)$ to be the durations $T_{dur,k}$ themselves as

$$y_{\text{target}}(k) = T_{dur,k} = s_{\text{in}}(k). \quad (17)$$

We substitute outputs $y_{\text{out}}(k)$ in Eq. (15) and targets $y_{\text{target}}(k)$ in Eq. (17) into Eq. (3), and then use Eq. (4) to

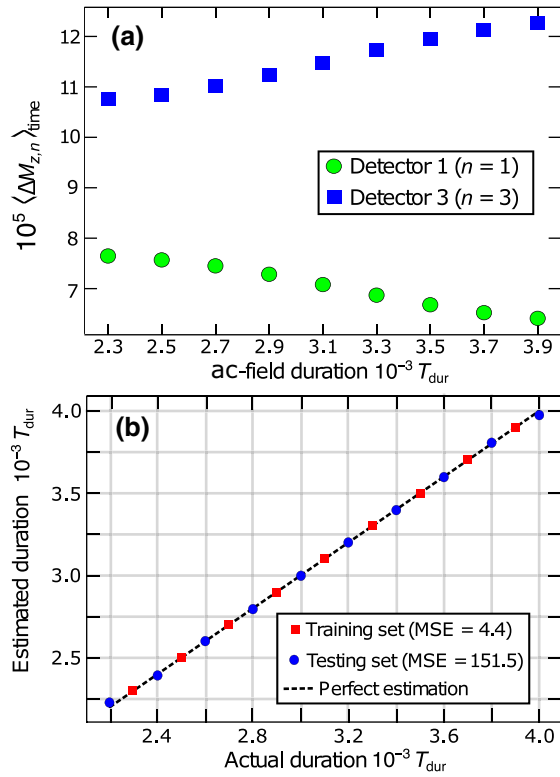


FIG. 4. (a) Temporal averages of dynamical magnetizations $\langle \Delta M_{z,n}(T_{\text{dur},k}) \rangle_{\text{time}}$ at detectors 1 and 3 ($n = 1$ and 3) over the time ranges indicated by shaded areas in Figs. 3(b1) and 3(b3) as functions of the duration of the ac magnetic field for the training dataset. We adopt a polynomial form with respect to $\langle \Delta M_{z,1}(T_{\text{dur},k}) \rangle_{\text{time}}$ and $\langle \Delta M_{z,3}(T_{\text{dur},k}) \rangle_{\text{time}}$ in Eq. (15) for output $y_{\text{out}}(k)$. (b) Results of the duration-estimation task. The horizontal (vertical) axis labels the actual (estimated) duration T_{dur} for both the training (red squares) and testing (blue circles) datasets. The dashed line with a slope of unity is the perfect estimation line for reference, indicating that amazingly accurate estimations are achieved.

obtain the optimal weight vector $\mathbf{W}_{\text{out}}^{\text{opt}}$, which minimizes the MSE for the training dataset. After this training procedure, we substitute $\mathbf{W}_{\text{out}}^{\text{opt}}$ into Eq. (15) to estimate the durations $T_{\text{dur},\ell}$ for the ten testing data of $T_{\text{dur},\ell} = 2200 + 200\ell$ with $\ell = 0, 1, \dots, 9$ as well as the nine training data of $T_{\text{dur},k} = 2300 + 200k$ with $k = 0, 1, \dots, 8$.

In Fig. 4(b), we show a plot of the estimated durations (outputs) versus the actual durations (inputs). Here the dashed line with a slope of unity is the perfect-estimation line. The plot shows amazingly accurate estimations for both the training and testing datasets. Surprisingly, the MSE turns out to be as small as 151.5 for the testing dataset. Considering that the square of the input values is of the order of about 10^6 , we find that this MSE value is extremely small. We take the root mean square error (RMSE) divided by the input average as a dimensionless quantity to represent the accuracy of estimations. Since the

average of durations for the testing dataset is 3100, this quantity is evaluated to be $\sqrt{151.5}/3100 \sim 0.004$. This value is one order of magnitude smaller than that of another previously proposed spin-wave reservoir based on a ferromagnetic garnet film [27]. In that work, it was assumed that the spin waves are excited by locally changing the uniaxial magnetic anisotropy and are exploited as reservoir states to estimate the durations of anisotropy change. According to Fig. 10 of Ref. [27], their RMSE divided by the input average of this garnet-based spin-wave reservoir can be roughly estimated to be about 0.08. The present result demonstrates that our skyrmion spin-wave reservoir harbors a great generalization ability to estimate the unknown ac-field durations in the testing dataset and possesses high potential for application to machine-learning information processing.

We now discuss a possible limitation in the generalization ability of our skyrmion spin-wave reservoir, that is, it might be difficult to correctly estimate widely ranging durations with our skyrmion system. More specifically, in order to correctly evaluate a certain duration, the weight vector \mathbf{W}_{out} should be trained by using a set of training data for the corresponding duration range. Namely, the weight vector \mathbf{W}_{out} trained by the data for intermediate durations can correctly estimate intermediate durations, but it might not be able to estimate longer or shorter durations. This is because the duration dependence of the behavior of magnetization dynamics varies depending on the duration range. To see this aspect, we compare the time profiles of $\Delta M_{z,2}(T_{\text{dur}}, t)$ for the longer durations in Fig. 3(c2) and those for the intermediate durations in Fig. 3(b2). The magnetization $\Delta M_{z,2}(T_{\text{dur}}, t)$ for the longer durations in Fig. 3(c2) monotonically decreases with increasing T_{dur} in the time range $800 \leq t \leq 1300$ (range A_c), whereas it monotonically increases in the subsequent time range $1300 \leq t \leq 1750$ (range B_c). These behaviors are opposite to the above-argued behaviors of $\Delta M_{z,2}(T_{\text{dur}}, t)$ for the intermediate durations in Fig. 3(b2). Therefore, the weight vector \mathbf{W}_{out} optimized for the intermediate durations might not be able to estimate the shorter or longer durations correctly. In practical experiments, it might be required to presume or restrict the range of durations.

We have numerically checked that, for other positions of the detectors, such as the nine detectors labeled 1 to 9 in Fig. 5(b), the out-of-plane magnetization responses also show similar monotonic behaviors with respect to the ac-field durations as in Fig. 3. Therefore, the highly accurate prediction of ac-field durations is expected to be achieved by different detectors set on the skyrmion lattice in experiments.

B. Short-term memory task and parity-check task

Next we examine the short-term memory (STM) task and the parity-check (PC) task [23,26]. By imposing the

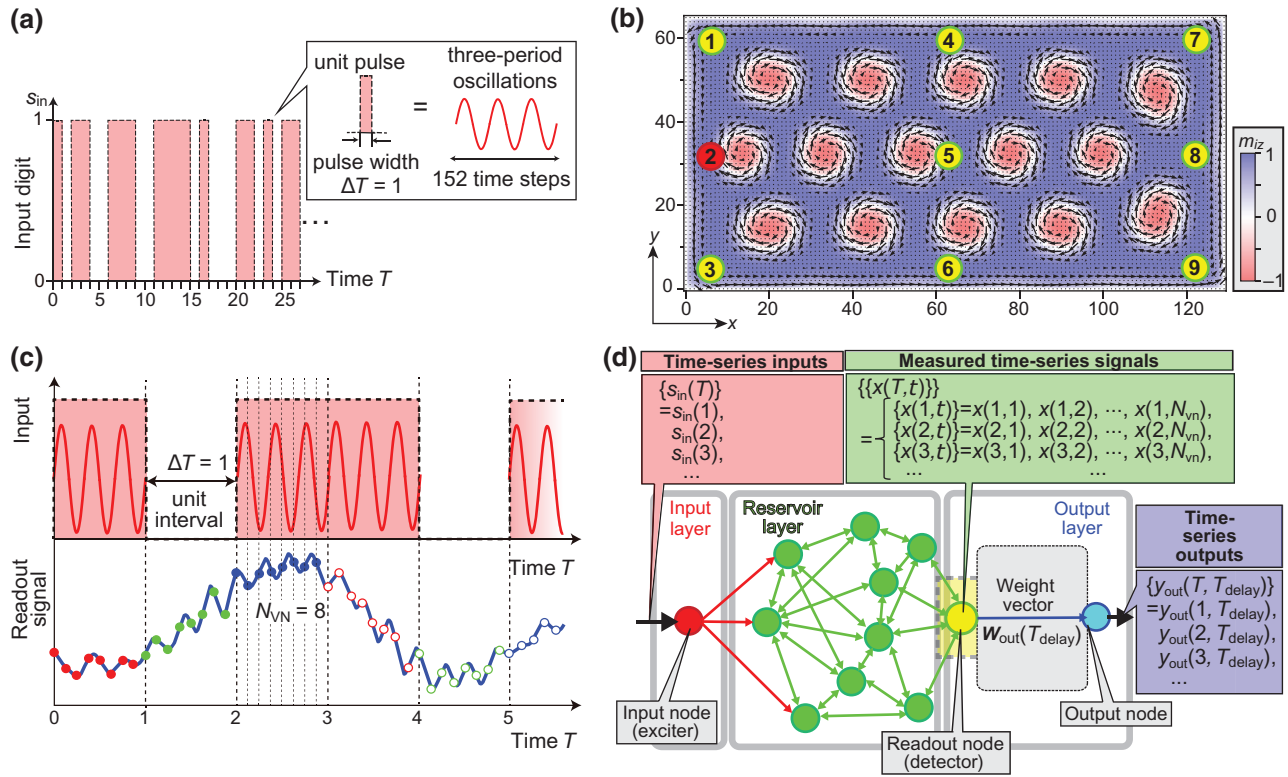


FIG. 5. (a) Schematics of the random time sequence of binary digits “1” and “0” as input signals used for the STM and PC tasks. The input “1” is represented by a pulse of three-period oscillations of the ac magnetic field, while the input “0” is represented by turning off the ac magnetic field for the same duration. The duration of the pulse is 152 integer time steps for integration of the LLG equation, which is chosen as a unit of time. (b) Setup of the input node (red circle) and readout nodes (red circle and green circles) on the skyrmion spin-wave reservoir used for the STM and PC tasks. Each node area has a radius of 3, in units of the lattice constant, and contains 32 sites inside it. For the readout nodes, nine different positions labeled 1 to 9 are examined. The red circle labeled 2 is assigned to both input and readout nodes. (c) Concept of the virtual nodes. For each time T , the unit interval of $\Delta T = 1$ from T to $T + 1$ that corresponds to the pulse width is divided into N_{VN} (equal to 8 in the present figure) moments with equivalent intervals. The signals are measured at N_{VN} moments at the readout node, which constitute the $(N_{VN} + 1)$ -dimensional reservoir state vector $\mathbf{x}(T)$. (d) Reservoir computing procedures for the STM and PC tasks.

STM task, we evaluate the short-term memory function of our skyrmion spin-wave reservoir, i.e., how long the reservoir can memorize the information of a past input sequence. This property is crucially important to analyze time-series data for, e.g., market forecasts, sentence predictions, and voice and speech recognition [1–3]. On the other hand, by imposing the PC task, we evaluate the ability of our reservoir to nonlinearly transform the input signals into readout signals. This property is indispensable to solve linearly inseparable problems [1–3,71] through mapping the input data onto a higher-dimensional information space for, e.g., pattern classifications and handwritten digit recognition [71].

For both tasks, the input data $s_{in}(T)$ are time-series binary digits of “1” and “0,” each of which is chosen randomly at every integer time T [Fig. 5(a)]. When the input digit is “1” at time T , we locally apply a pulse of three-period oscillations of the ac magnetic field, the duration of which corresponds to 152 integration time steps of the

LLG equation. The magnetic field pulse is applied within the red circular area labeled 2 in Fig. 5(b), the center of which is located at $(x, y) = (6.5, 32.5)$. On the other hand, when the input digit is “0,” we turn off the ac magnetic field and let the magnetizations relax for the same duration of 152 integration time steps. Here the integer time T is counted in units of this three-period duration.

We define the desired outputs y_{target} in Eq. (3) for respective tasks as

$$y_{target}^{STM}(T, T_{delay}) = s_{in}(T - T_{delay}), \quad (18)$$

$$y_{target}^{PC}(T, T_{delay}) = \text{mod}[s_{in}(T) + s_{in}(T - 1) + \dots + s_{in}(T - T_{delay}), 2], \quad (19)$$

where T_{delay} is an integer variable that represents a given delay time. The STM task examines to what extent the input signal at a previous time $T - T_{delay}$ can be reconstructed from the current reservoir states at time T . On the

other hand, the PC task examines to what extent the reservoir can describe nonlinear functions by taking parity of the sum of past binary inputs from current time T to a previous time $T - T_{\text{delay}}$ as a typical example of nonlinear functions. Mapping of the input data onto a high-dimensional information space via nonlinear transformations is a key function of the reservoir, and it must be carried by the reservoir instead of the output layer because the output layer in reservoir computing simply produces outputs by a linear combination of the reservoir states [1–3].

Here we consider only one readout node for both tasks. In the reservoir computing, we need multiple readout data for a certain input to construct a reservoir state vector. In the examination of the duration-estimation task, we measured signals at multiple readout nodes, i.e., detectors 1 and 3 [Fig. 2(a)] to prepare the multiple readout data. In the present examinations, instead of measuring signals at multiple readout nodes, we measure signals from a single readout node at multiple moments during the interval from T to $T + 1$, and regard the measured sequential data as the components of the reservoir state vector at time T . Specifically, we divide each unit interval of pulse $\Delta T = 1$, i.e., a duration of the three-period oscillations of the ac magnetic field, into N_{VN} moments with equivalent intervals, which are referred to as virtual nodes [Fig. 5(c)]. We simulate time evolutions of the magnetizations \mathbf{m}_i by solving the LLG equation and trace the time profile of site-averaged z -component magnetization $M_z(T, \tau)$ inside the readout node. Here the average is taken over sites within the circular area of the detector, and the integer variable $\tau (= 1, 2, \dots, N_{\text{VN}})$ is an index of the virtual nodes. As a position of the single readout node, we examine nine circular areas as its candidates to investigate possible dependence of the performance on the position of the readout node. The candidate positions are labeled 1 to 9, as shown in Fig. 5(b). Note that the position labeled 2 is assigned to both the input node and a readout node. The radii of the circular detector areas are all 3, in units of the lattice constant. The center of detector 5 is located at $(x, y) = (64.5, 32.5)$, and the centers of neighboring detectors are separated by distances of 58 and 26, in units of the lattice constant, along the x and y axes, respectively.

The reservoir computing procedures for the STM and PC tasks are as follows [see also Fig. 5(d)]. We first construct the reservoir state vector $\mathbf{x}(T)$ for each time step T . The vector $\mathbf{x}(T)$ is composed of signals $M_z(T, \tau)$ measured at the readout node during the time interval from T to $T + 1$ as

$$\mathbf{x}(T) = \begin{pmatrix} x_0 \\ M_z(T, 1) \\ M_z(T, 2) \\ \vdots \\ M_z(T, N_{\text{VN}}) \end{pmatrix} \quad (20)$$

with

$$M_z(T, \tau) = \frac{1}{N_{\text{detect}}} \sum_{i \in \text{detector}} m_{z,i}(T, \tau), \quad (21)$$

where τ is the index of virtual nodes, and $N_{\text{detect}} (= 32)$ is the number of sites inside the area of the detector. A constant bias $x_0 = 1$ is included as the first component of the vector $\mathbf{x}(T)$. Thus, the dimension of $\mathbf{x}(T)$ is $N_{\text{VN}} + 1$. The constructed reservoir state vectors are translated to output $y_{\text{out}}(T, T_{\text{delay}})$ for a given delay T_{delay} by a linear transformation with weight vector $\mathbf{W}_{\text{out}}(T_{\text{delay}})$ as

$$\begin{aligned} y_{\text{out}}(T, T_{\text{delay}}) &= \mathbf{W}_{\text{out}}(T_{\text{delay}}) \cdot \mathbf{x}(T) \\ &= W_0 + W_1 M_z(T, 1) + W_2 M_z(T, 2) \\ &\quad + \dots + W_{N_{\text{VN}}} M_z(T, N_{\text{VN}}), \end{aligned} \quad (22)$$

where

$$\mathbf{W}_{\text{out}}(T_{\text{delay}}) = (W_0(T_{\text{delay}}), W_1(T_{\text{delay}}), \dots, W_{N_{\text{VN}}}(T_{\text{delay}})). \quad (23)$$

Note that the weight vectors $\mathbf{W}_{\text{out}}(T_{\text{delay}})$ differ among the delay times T_{delay} and among the nine detector positions. They are required to be trained independently for each delay time and for each detector position.

Figures 6(a)–6(i) show time profiles of the dynamical magnetizations measured at detectors 1–9 as responses to the first 30 random sequences of 1/0 input digits, which are respectively entered via the input node by turning the ac-field pulses on and off. The unit pulse consists of three-period oscillations of the ac magnetic field, the duration of which corresponds to 152 time steps in the LLG integration. The horizontal axis represents the integer time T in units of the pulse width. The left vertical axes represent the ac-field pulses being turned on or off. The right vertical axes represent rescaled magnetization $\Delta M_z(t)$ measured at each detector, which is defined by $\Delta M_z(t) \equiv [M_z(t) - M_z^{\text{min}}] \times 10^5$. Here M_z^{min} is the minimum value of $M_z(t)$ in the initial 380 pulse units, and $M_z(t) \equiv \sum_i m_{zi}(t)/N_{\text{detect}}$ is the magnetization averaged over the detector area.

In Fig. 6(b) for detector 2, each shaded unit bar contains three oscillations of $\Delta M_z(t)$ because detector 2 is also the input node to which the ac-field pulse is applied, and the magnetizations in this area respond instantaneously to the applied ac magnetic field. In Figs. 6(a) and 6(c) for detectors 1 and 3, the magnetizations $\Delta M_z(t)$ also respond almost instantaneously to the ac-field pulses being turned on or off because the locations of these detectors are also close to the input node (detector 2). On the contrary, in Figs. 6(d)–6(i) for distant detectors 4–9, the magnetization oscillations are weaker in amplitude and exhibit certain delays with respect to the timing of the input. For example, in the first interval from $T = 0$ to $T = 1$, the magnetizations start oscillating only near the end of this time interval,

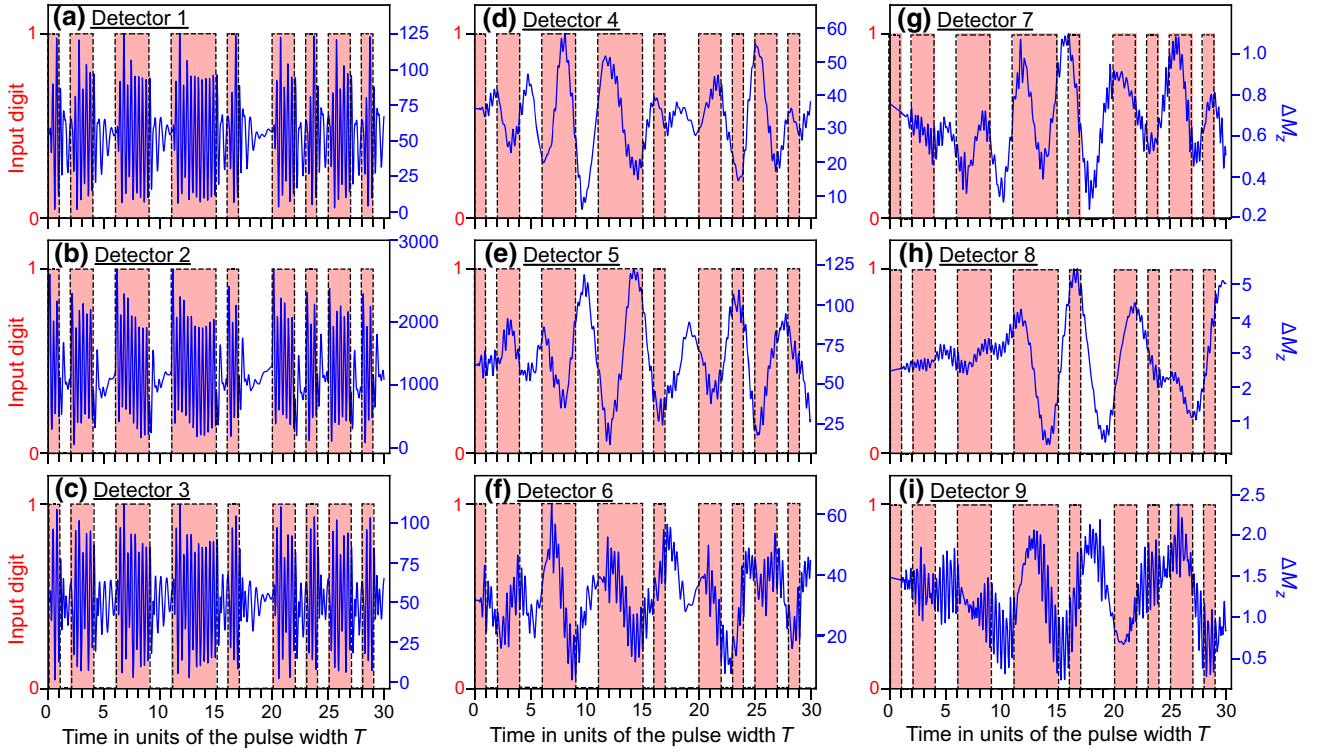


FIG. 6. (a)–(i) Time profiles of the dynamical magnetization $\Delta M_z(t)$ measured at detectors 1–9 as responses to the first 30 random sequences of on-off ac-field pulses. A single ac-field pulse is composed of three-period oscillations of the ac magnetic field, and its duration is chosen as a unit of time. The shaded rectangles and blanks in each panel indicate the time series of input digits “1” and “0” injected into the reservoir by turning the ac-field pulses on and off, respectively.

even though the ac-field pulse is applied to the input node (detector 2) from the beginning in this time interval. It is also worth noting that the overall envelopes of the magnetization oscillations at these distant detectors are less correlated with the input sequence compared to those at the detectors close to the input, i.e., detectors 1–3.

The analyses of the STM (PC) task are done as follows. Target $y_{\text{target}}(T, T_{\text{delay}})$ in Eq. (18) [Eq. (19)] and output $y_{\text{out}}(T, T_{\text{delay}})$ are substituted into the formula for the MSE in Eq. (3) and we optimize the weight matrix for respective detectors by the pseudoinverse-matrix method using a sequence of input data for training. After this training procedure, a subsequent sequence of input data for testing are entered to investigate the performance of the reservoir on the STM and PC tasks.

In Figs. 7(a)–7(d), we compare the profiles of output $y_{\text{out}}(T, T_{\text{delay}})$ (blue dashed lines) with those of target $y_{\text{target}}(T, T_{\text{delay}})$ (red solid lines) for the STM task for several choices of delay T_{delay} , i.e., (a) $T_{\text{delay}} = 1$, (b) $T_{\text{delay}} = 2$, (c) $T_{\text{delay}} = 7$, and (d) $T_{\text{delay}} = 10$. Here the profiles of the targets are calculated using Eq. (18), and the measurements of the readout signals are performed at detector 7 by setting the number of virtual nodes $N_{\text{VN}} = 62$. We find that the outputs perfectly reproduce the targets when the

delay is as small as $T_{\text{delay}} = 1$ and $T_{\text{delay}} = 2$ in Figs. 7(a) and 7(b), respectively. On the contrary, when T_{delay} is relatively large as $T_{\text{delay}} = 7$ and $T_{\text{delay}} = 10$, the discrepancies are pronounced although the tendencies of the targets are reproduced to some extent [Figs. 7(c) and 7(d)].

We also compare the profiles of output $y_{\text{out}}(T, T_{\text{delay}})$ with those of target $y_{\text{target}}(T, T_{\text{delay}})$ for the PC task in Figs. 8(a)–8(c) for selected delays T_{delay} , i.e., (a) $T_{\text{delay}} = 1$, (b) $T_{\text{delay}} = 2$, and (c) $T_{\text{delay}} = 7$. Here the profiles of the target are calculated using Eq. (19), and the measurements of the readout signals are again performed by setting $N_{\text{VN}} = 62$. Figure 8(a) shows perfect coincidence between the outputs and the targets when $T_{\text{delay}} = 1$. However, discrepancy appears even when the delay is as small as $T_{\text{delay}} = 2$ [Fig. 8(b)], and becomes more significant when $T_{\text{delay}} = 7$ [Fig. 8(c)].

To quantitatively evaluate the performance, we use the standard squared correlation Corr^2 between the targets and the outputs defined by [23,26,72]

$$\text{Corr}^2(T_{\text{delay}}) = \frac{\text{Cov}^2[y_{\text{target}}(T, T_{\text{delay}}), y_{\text{out}}(T, T_{\text{delay}})]}{\text{Var}[y_{\text{target}}(T, T_{\text{delay}})] \text{Var}[y_{\text{out}}(T, T_{\text{delay}})]} \quad (24)$$

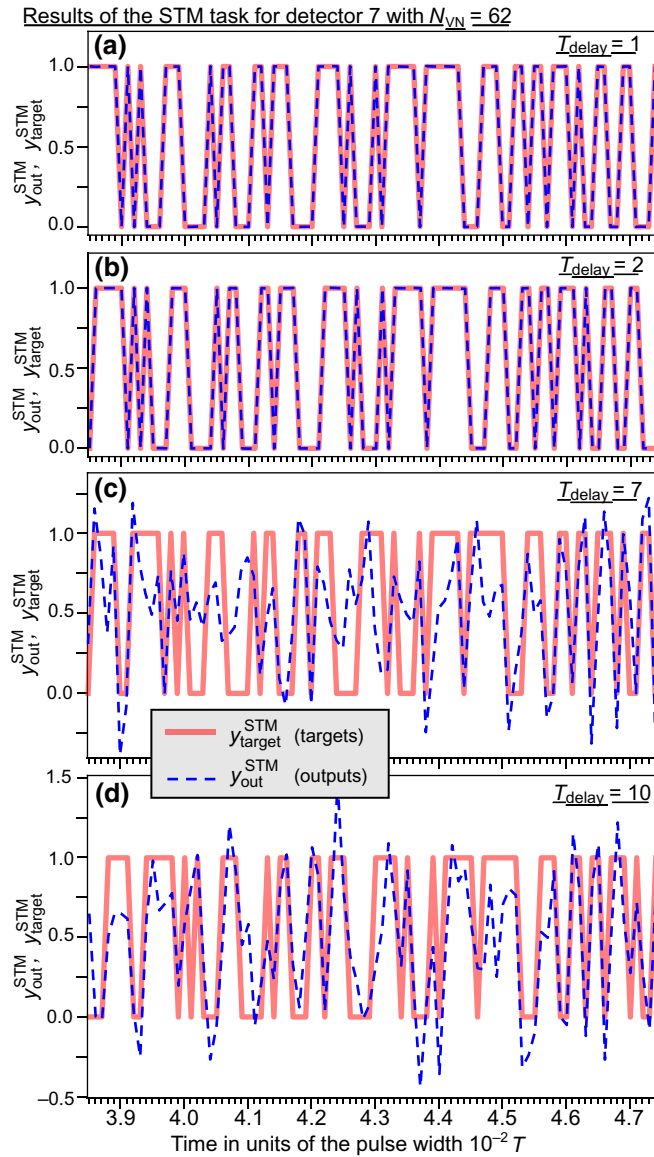


FIG. 7. Comparison between profiles of output $y_{\text{out}}(T, T_{\text{delay}})$ (blue dashed lines) and those of target $y_{\text{target}}(T, T_{\text{delay}})$ (red solid lines) for the STM task for various delays T_{delay} , i.e., (a) $T_{\text{delay}} = 1$, (b) $T_{\text{delay}} = 2$, (c) $T_{\text{delay}} = 7$, and (d) $T_{\text{delay}} = 10$. The profiles of the target are calculated using Eq. (18), and the analyses are performed by measuring the magnetization data at detector 7 and setting the number of virtual nodes $N_{\text{VN}} = 62$.

with

$$\text{Cov}[A(T), B(T)] = \frac{1}{N_T} \sum_T (A(T) - \bar{A})(B(T) - \bar{B}),$$

$$\text{Var}[A(T)] = \frac{1}{N_T} \sum_T (A(T) - \bar{A})^2,$$

where Cov and Var denote the covariance and variance, respectively, \bar{A} is the average of $A(T)$ over all T , and N_T is

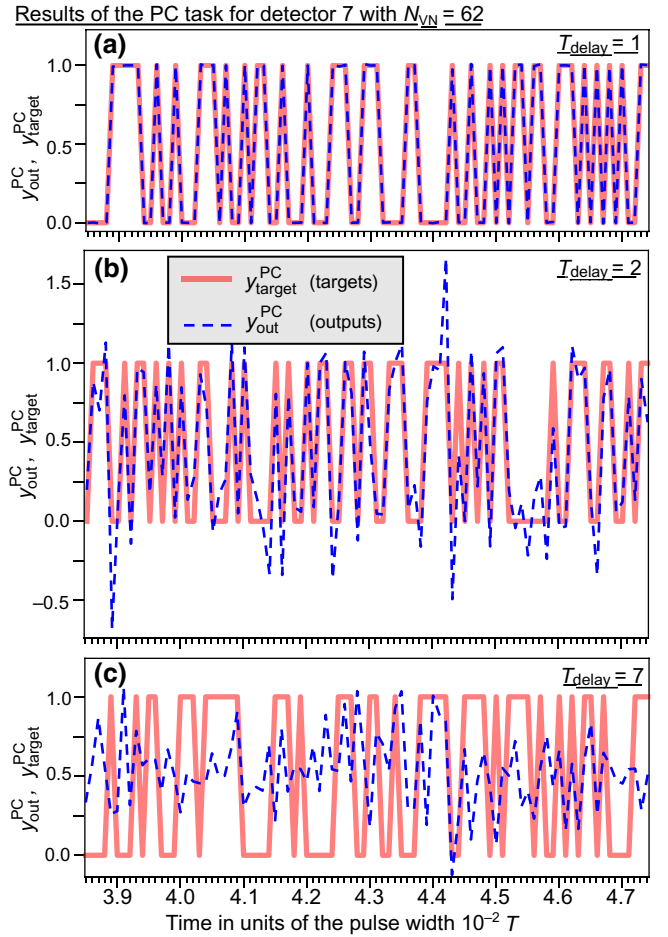


FIG. 8. Comparison between profiles of output $y_{\text{out}}(T, T_{\text{delay}})$ (blue dashed lines) and those of target $y_{\text{target}}(T, T_{\text{delay}})$ (red solid lines) for the PC task for various delays T_{delay} , i.e., (a) $T_{\text{delay}} = 1$, (b) $T_{\text{delay}} = 2$, and (c) $T_{\text{delay}} = 7$. The profiles of the target are calculated using Eq. (19), and the analyses are performed by measuring the magnetization data at detector 7 and setting the number of virtual nodes $N_{\text{VN}} = 62$.

the number of time steps T . The standard squared correlation Corr^2 takes a value within the range $[0, 1]$, and a larger value indicates better coincidence of the outputs with the targets. In the present analysis, this quantity is calculated using a sequence of 90 binary digits for testing after optimizing the weight matrix using a sequence of 350 binary digits for training. After calculating Corr^2 as a function of T_{delay} , we take their summation over a specific range of T_{delay} to evaluate a quantity called the capacity C for both the STM and PC tasks [23,26,72],

$$C = \sum_{T_{\text{delay}}=0}^{T_{\text{delay}}^{\text{max}}} \text{Corr}^2(T_{\text{delay}}). \quad (25)$$

A larger capacity indicates that a larger amount of memory or nonlinearity is stored in the current reservoir state.

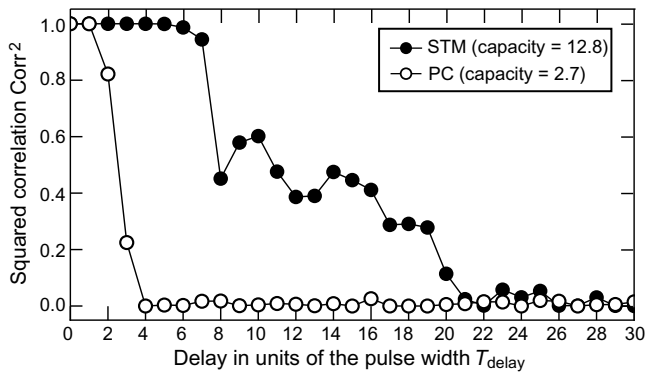


FIG. 9. Squared correlations, Corr^2 , of the STM (filled circles) and PC (open circles) tasks as functions of the delay time T_{delay} for detector 7. Capacities of the STM and PC tasks, C_{STM} and C_{PC} , which correspond to areas below the respective curves, quantify the performance of the reservoir for these tasks. The measurements of signals are performed by setting the number of virtual nodes $N_{\text{VN}} = 62$.

Therefore, the capacity can quantify the performance of reservoir for the STM and PC tasks.

Figure 9 presents the calculated squared correlations Corr^2 for the STM and PC tasks as functions of the delay T_{delay} for detector 7. Here the examinations of both tasks are done by setting the number of virtual nodes $N_{\text{VN}} = 62$. The squared correlation Corr^2 for the STM task is nearly unity from $T_{\text{delay}} = 0$ to $T_{\text{delay}} = 6$, in accordance with the nearly perfect coincidence between the outputs and the targets when $T_{\text{delay}} = 1$ [Fig. 7(a)] and $T_{\text{delay}} = 2$ [Fig. 7(b)]. However, it starts decreasing from $T_{\text{delay}} = 7$ and gradually decays as T_{delay} increases in accordance with the apparent discrepancy between the outputs and the targets at $T_{\text{delay}} = 7$ [Fig. 7(c)] and $T_{\text{delay}} = 10$ [Fig. 7(d)]. The squared correlation Corr^2 for the STM task finally vanishes around $T_{\text{delay}} = 22$. We note that this fading memory property (also known as the echo-state property [72]) is essential for a workable reservoir, since it indicates that the reservoir states can be independent of the initial configuration of the physical system, after the injection of a long enough input sequence [1]. On the other hand, Corr^2 for the PC task shows much steeper decrease. Namely, it is nearly unity only at $T_{\text{delay}} = 0$ and $T_{\text{delay}} = 1$, but becomes suppressed abruptly (about 0.8 at $T_{\text{delay}} = 2$ and about 0.2 at $T_{\text{delay}} = 3$). This is consistent with the considerable discrepancy between the outputs and the targets even at $T_{\text{delay}} = 2$ in Fig. 8(b). The squared correlation Corr^2 for the PC task vanishes at $T_{\text{delay}} = 4$.

Because the squared correlations Corr^2 for the STM and PC tasks decay as T_{delay} increases and almost vanish above $T_{\text{delay}} = 22$ and $T_{\text{delay}} = 4$, respectively (Fig. 9), we set $T_{\text{delay}}^{\text{max}} = 30$ in Eq. (25) to evaluate the capacities for these tasks. Figure 10 shows the capacities for both STM and PC

tasks, C_{STM} and C_{PC} , as functions of the number of virtual nodes N_{VN} for respective detectors. For all the detectors, both C_{STM} and C_{PC} increase nearly monotonically as N_{VN} increases because larger N_{VN} endows more degrees of freedom in the weight matrix to describe the output data. Both capacities are saturated to certain values. The largest C_{STM} and C_{PC} are about 12.8 and 2.7, respectively. These values are comparable with those of other previously proposed spintronics reservoirs under a similar number of virtual nodes [23,26,28], which clearly demonstrates that the magnetic skyrmion system is promising for application to the physical reservoir.

To investigate possible detector-position dependence of the performance, in Fig. 11 we compare the capacities C_{STM} and C_{PC} for different detectors by plotting the data for specified numbers of virtual nodes, i.e., $N_{\text{VN}} = 1, 25, 50, 75$, and 100, extracted from Fig. 10. We use red, green, and blue symbols to represent detectors 1–3, 4–6, and 7–9, respectively, which are categorized in terms of their positions. Specifically, detectors 1–3 represented by red symbols are located near the left edge of the rectangular-shaped system and are thus close to or exactly on the input node, whereas detectors 7–9 represented by blue symbols are located near the right edge and are thus far from the input node. Detectors 4–6 represented by green symbols are located in the middle of the system with intermediate distances from the input node. We find that there are apparent dependencies on the detector position for both C_{STM} and C_{PC} , but their tendencies are opposite.

The plots in Fig. 11(a) show that the capacities C_{STM} abruptly increase as N_{VN} increases from $N_{\text{VN}} = 1$ to $N_{\text{VN}} = 25$ and saturate to certain constant values above $N_{\text{VN}} = 50$ for all the detectors. We also find that there is an apparent trend that the detectors distant from the input node exhibit better performance on the STM task as indicated by larger values of C_{STM} . Indeed, detectors 7–9 located near the right edge (blue symbols) tend to have larger C_{STM} , while detectors 1–3 located near the left edge (red symbols) tend to have smaller C_{STM} .

On the other hand, the capacities C_{PC} show similar abrupt increase and saturating behavior in Fig. 11(b). However, the trend of the detector-position dependence is opposite to that of C_{STM} . Apparently, the detectors closer to the input node tend to exhibit better performance with larger C_{PC} for the PC task and can thus achieve more significant nonlinearity in response. Indeed, detectors 1–3 (red symbols) have larger C_{PC} than detectors 7–9 (blue symbols).

The observed opposite trends of the detector-position dependence between the two capacities C_{STM} and C_{PC} seem to be consistent with an empirical law of the memory-nonlinearity trade-off relation in dynamical models [73,74]. It was argued that the memory capacity seems to be degraded by introducing nonlinearity into the dynamics in reservoirs and vice versa. Clarification of possible

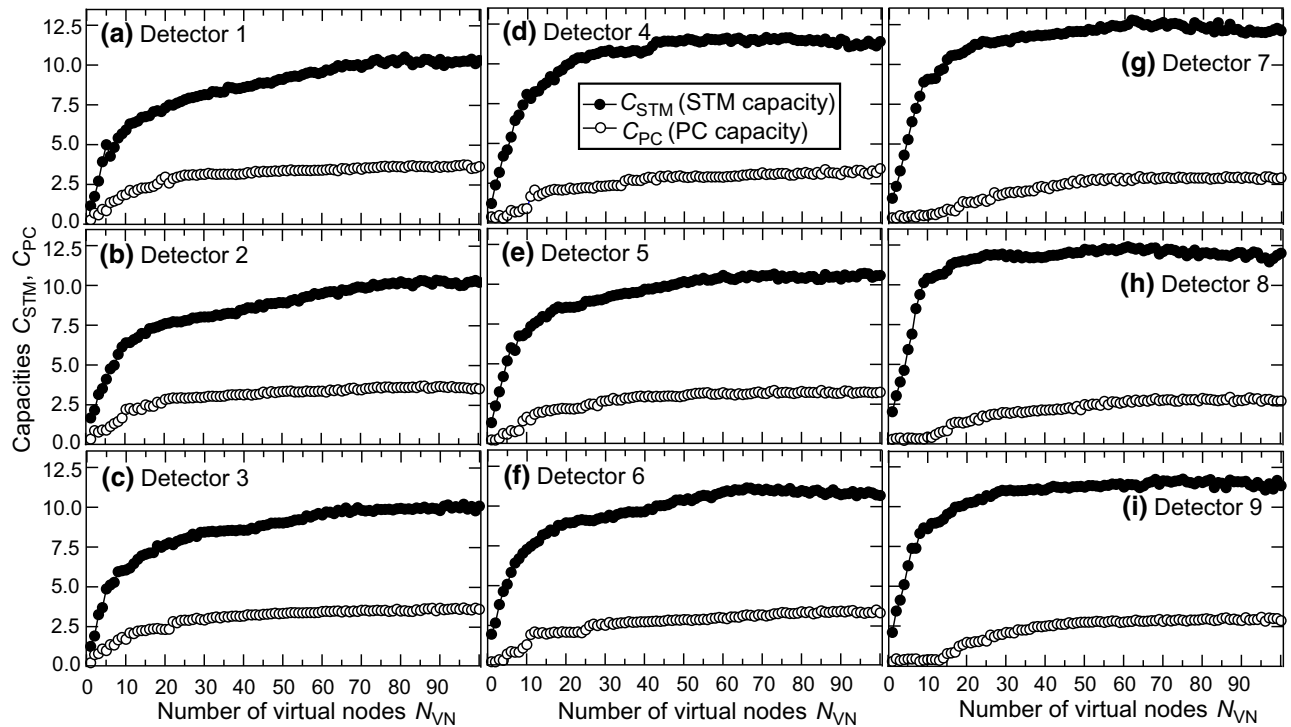


FIG. 10. Capacities of STM (filled circles) and PC (open circles) tasks, C_{STM} and C_{PC} , as functions of the number of virtual nodes N_{VN} for respective detectors. The capacities correspond to summations of the squared correlations, Corr^2 , over the range $0 \leq T_{\text{delay}} \leq 30$ for 90 testing data, after optimizing the weight matrix using 350 training data. For our skyrmion spin-wave reservoir, the largest values of C_{STM} and C_{PC} are 12.8 and 2.7, respectively.

connection of the magnetic skyrmion system with the dynamical systems are left for future studies.

We have investigated the performance of the skyrmion spin-wave reservoir on the STM and PC tasks by taking the three-period ac-field pulse as an input unit. To study possible pulse-width dependence of the performance, we calculate the capacities C_{STM} and C_{PC} using pulses with different widths, i.e., single-period and five-period ac-field pulses. We employ the same random sequence of binary inputs as that used in the examination with the three-period ac-field pulses. For this comparison, we use initial 150 binary data for training and subsequent 50 binary data for testing. The capacities C_{STM} and C_{PC} are again calculated by summing up the squared correlations Corr^2 in the range $0 \leq T_{\text{delay}} \leq 30$.

Figures 12(a) and 12(b) show the calculated pulse-width dependencies of C_{STM} and C_{PC} , respectively. Here the number of virtual nodes is fixed at $N_{\text{VN}} = 50$. The colored symbols are assigned to respective detectors depending on the distance from the input node in the same fashion as in Fig. 11. According to this figure, the pulse-width dependence also exhibits some characteristic behaviors. For the capacity C_{STM} , the detectors relatively distant from the input node, i.e., detectors 4–7 (green and blue symbols), tend to exhibit larger values than the close detectors, i.e., detectors 1–3. In particular, detector 7 (blue circles)

exhibits the largest value of $C_{\text{STM}}^{\text{max}} \sim 13$, and detector 4 (green circles) exhibits the second largest value of $C_{\text{STM}}^{\text{max}} \sim 12$ when the pulse width is one period of the ac magnetic field. However, the values for these two detectors decrease as the pulse width increases, indicating that we can obtain a better performance on the STM task with a shorter pulse and a detector distant from the input node.

However, we should note that detectors located distant from the input node do not necessarily exhibit high performance on the STM task. For example, detectors 8 and 9 (blue triangles and squares) exhibit lower or comparable values of C_{STM} than detectors 4 and 5 at the intermediate distance when the pulse widths are one and three periods. Moreover, detector 6 exhibits almost the lowest values when the pulse width is one period despite it being located at the intermediate distance. We realize that both detectors 6 and 9 with low performance are located near the bottom edge of the rectangular system, whereas both detectors 4 and 7 with high performance are located near the upper edge. It is known that the spin waves in magnetic skyrmions are subject to emergent magnetic fields generated by the magnetizations of topological skyrmion textures, which cause their transverse propagation called the topological magnon Hall effect. Because of this effect, the propagation of spin waves in the skyrmion spin-wave reservoir can be directional and their amplitude

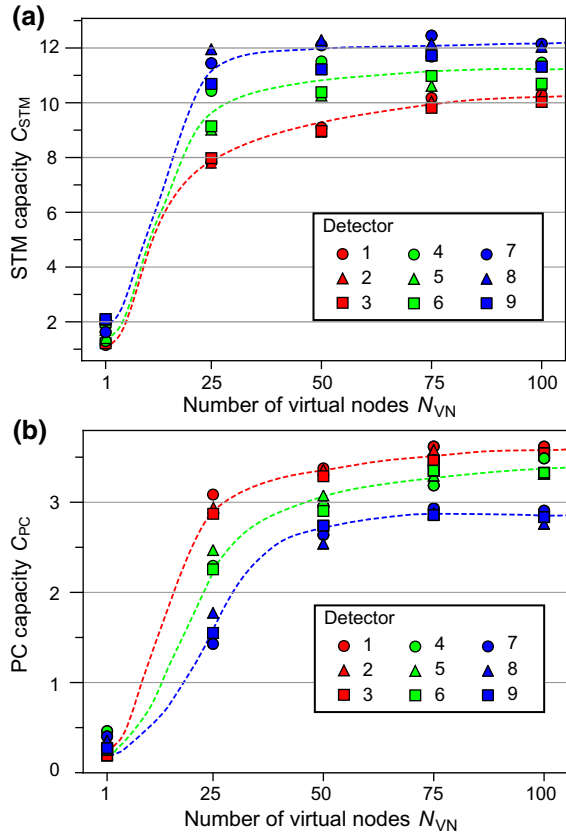


FIG. 11. (a) The N_{VN} dependence of the STM capacity C_{STM} for respective detectors, where N_{VN} is the number of virtual nodes. (b) The N_{VN} dependence of the PC capacity C_{PC} . Detectors 1–9 are located at the positions shown in Fig. 5(b). Symbol colors categorize these detectors in terms of the distance from the input node. Specifically, red is assigned to detectors 1–3 located near the left edge in Fig. 5(b) close to the input node, whereas blue is assigned to detectors 7–9 located near the right edge distant from the input node. Green is assigned to detectors 4–6 located in the middle of the system where the distances from the input node are intermediate. Dashed lines are visual guides.

distribution can be asymmetric, which may lead to the observed distinct performance between detectors near the upper edge and those near the bottom edge.

On the other hand, the plots of C_{PC} in Fig. 12(b) show no significant dependence on the pulse width for detectors 1–3 (red symbols) and detectors 4–6 (green symbols). The values are almost constant at $C_{PC} = 3$ –3.6 irrespective of the pulse width for these detectors. On the contrary, for detectors 7–9 (blue symbols), the values are considerably smaller, $C_{PC} = 0.5$ –1.5, when the pulse width is as short as one period. The performance of detectors 7 and 9 for the PC task is remarkably low ($C_{PC} \sim 0.5$ when the pulse width is one period). This fact seems to be in sharp contrast to the case of the STM task discussed above. Namely, the largest capacity of the STM task ($C_{STM} \sim 13$) is achieved by detector 7 when the pulse width is one period. The contrasting performance for detector 7

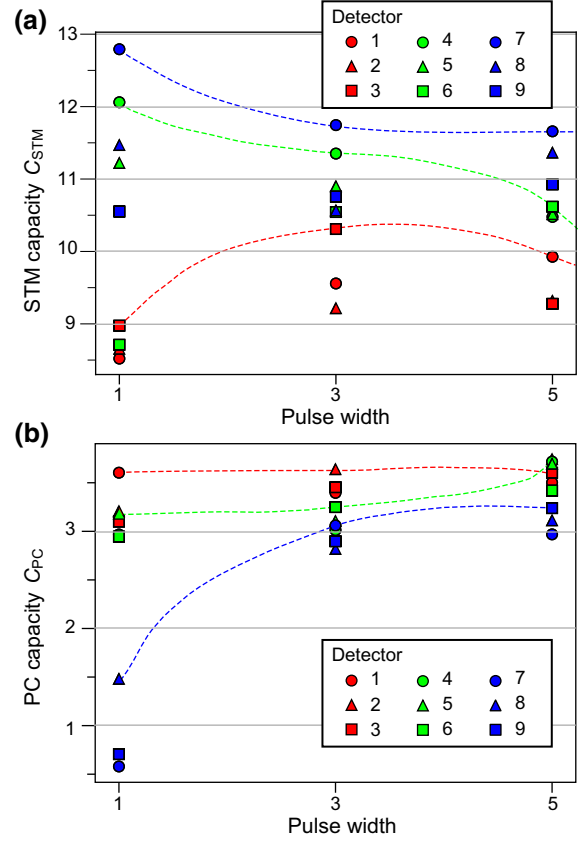


FIG. 12. Pulse-width dependence of (a) STM capacity C_{STM} and (b) PC capacity C_{PC} . The pulse width along the x axis is in units of the period of the ac magnetic field, which is roughly $2\pi/0.12416 \approx 50.6$. For pulse widths equal to 1, 3, and 5, we take integer time steps of 51, 152, and 254, respectively, for the LLG integration. Detectors 1–9 are located at the positions shown in Fig. 5(b). The symbols are the same as those in Fig. 11. Dashed lines are visual guides.

between the STM and PC tasks seems to be consistent with the memory-nonlinearity trade-off relation in dynamical models again.

IV. CONCLUSION

In this paper, we propose a concept of the skyrmion spin-wave reservoir and examine its properties and performance. We investigate three of the required characteristics of the reservoir, i.e., the generalization ability, short-term memory function, and nonlinearity of our skyrmion spin-wave reservoir, by imposing three standard tasks, i.e., the duration-estimate task, short-term memory task, and parity-check task. Through these investigations, we demonstrate that the skyrmion spin-wave reservoir possesses high abilities for information processing. Importantly, magnetic skyrmions emerge spontaneously in magnetic specimens with broken spatial inversion symmetry under application of a static magnetic field via a self-organization process. Therefore, the proposed skyrmion

reservoir requires neither advanced nanofabrication nor complicated manufacturing for their production, in contrast to other previously proposed magnetic reservoirs with elaborate spintronics devices, e.g., spin-torque oscillators and magnetic tunnel junctions. Our proposal will necessarily pave a way to the realization of practically useful spintronics reservoirs of high performance.

ACKNOWLEDGMENTS

This work is supported by the Japan Society for the Promotion of Science KAKENHI (Grant No. 20H00337), CREST, the Japan Science and Technology Agency (Grant No. JPMJCR20T1), and a research grant in the natural sciences from the Mitsubishi Foundation.

-
- [1] G. Tanaka, T. Yamane, J. B. Héroux, R. Nakane, N. Kanazawa, S. Takeda, H. Numata, D. Nakano, and A. Hirose, Recent advances in physical reservoir computing: A review, *Neural Netw.* **115**, 100 (2019).
- [2] K. Nakajima, Physical reservoir computing: An introductory perspective, *Jpn. J. Appl. Phys.* **59**, 060501 (2020).
- [3] K. Nakajima and I. Fischer, Reservoir computing: Theory, physical implementations, and applications, *IEICE Tech. Rep.* **118**, 149 (2018).
- [4] R. J. Williams and D. Zipser, A learning algorithm for continually running fully recurrent neural networks, *Neural Comput.* **1**, 270 (1989).
- [5] P. J. Werbos, Backpropagation through time: What it does and how to do it, *Proc. IEEE* **78**, 1550 (1990).
- [6] Y. Paquot, F. Duport, A. Smerieri, J. Dambre, B. Schrauwen, M. Haelterman, and S. Massar, Optoelectronic reservoir computing, *Sci. Rep.* **2**, 1 (2012).
- [7] K. Vandoorne, W. Dierckx, B. Schrauwen, D. Verstraeten, R. Baets, P. Bienstman, and J. Van Campenhout, Toward optical signal processing using photonic reservoir computing, *Opt. Express* **16**, 11182 (2008).
- [8] F. Duport, B. Schneider, A. Smerieri, M. Haelterman, and S. Massar, All-optical reservoir computing, *Opt. Express* **20**, 22783 (2012).
- [9] J. Bueno, D. Brunner, M. C. Soriano, and I. Fischer, Conditions for reservoir computing performance using semiconductor lasers with delayed optical feedback, *Opt. Express* **25**, 2401 (2017).
- [10] G. Dion, S. Mejaouri, and J. Sylvestre, Reservoir computing with a single delay-coupled non-linear mechanical oscillator, *J. Appl. Phys.* **124**, 152132 (2018).
- [11] H. Hauser, A. J. Ijspeert, R. M. Füchslin, R. Pfeifer, and W. Maass, The role of feedback in morphological computation with compliant bodies, *Biol. Cybern.* **106**, 595 (2012).
- [12] K. Caluwaerts and B. Schrauwen, in *Proceedings of the 2nd International Conference on Morphological Computation (ICMC)* (Ghent University, Venice, 2011), p. 45.
- [13] K. Nakajima, H. Hauser, T. Li, and R. Pfeifer, Exploiting the dynamics of soft materials for machine learning, *Soft Robot.* **5**, 339 (2018).
- [14] K. Caluwaerts, J. Despraz, A. İşçen, A. P. Sabelhaus, J. Bruce, B. Schrauwen, and V. SunSpiral, Design and control of compliant tensegrity robots through simulation and hardware validation, *J. R. Soc. Interface* **11**, 20140520 (2014).
- [15] M. R. Dranias, H. Ju, E. Rajaram, and A. M. VanDongen, Short-term memory in networks of dissociated cortical neurons, *J. Neurosci.* **33**, 1940 (2013).
- [16] K. P. Dockendorf, I. Park, P. He, J. C. Príncipe, and T. B. DeMarse, Liquid state machines and cultured cortical networks: The separation property, *Biosystems* **95**, 90 (2009).
- [17] K. Nakajima, H. Hauser, R. Kang, E. Guglielmino, D. G. Caldwell, and R. Pfeifer, A soft body as a reservoir: Case studies in a dynamic model of octopus-inspired soft robotic arm, *Front. Comput. Neurosci.* **7**, 91 (2013).
- [18] C. Du, F. Cai, M. A. Zidan, W. Ma, S. H. Lee, and W. D. Lu, Reservoir computing using dynamic memristors for temporal information processing, *Nat. Commun.* **8**, 2204 (2017).
- [19] L. Appeltant, M. C. Soriano, G. Van der Sande, J. Danckaert, S. Massar, J. Dambre, B. Schrauwen, C. R. Mirasso, and I. Fischer, Information processing using a single dynamical node as complex system, *Nat. Commun.* **2**, 468 (2011).
- [20] Y. Zhang, P. Li, Y. Jin, and Y. Choe, A digital liquid state machine with biologically inspired learning and its application to speech recognition, *IEEE Trans. Neural Netw. Learn. Syst.* **26**, 2635 (2015).
- [21] M. S. Kulkarni and C. Teuscher, in *2012 IEEE/ACM international symposium on nanoscale architectures (NANOARCH)* (IEEE, Amsterdam, 2012), p. 226.
- [22] J. Torrejon, M. Riou, F. A. Araujo, S. Tsunegi, G. Khalsa, D. Querlioz, P. Bortolotti, V. Cros, K. Yakushiji, A. Fukushima, H. Kubota, S. Yuasa, M. D. Stiles, and J. Grollier, Neuromorphic computing with nanoscale spintronic oscillators, *Nature* **547**, 428 (2017).
- [23] T. Kanao, H. Suto, K. Mizushima, H. Goto, T. Tanamoto, and T. Nagasawa, Reservoir Computing on Spin-Torque Oscillator Array, *Phys. Rev. Appl.* **12**, 024052 (2019).
- [24] D. Marković, N. Leroux, M. Riou, F. Abreu Araujo, J. Torrejon, D. Querlioz, A. Fukushima, S. Yuasa, J. Trastoy, P. Bortolotti, and J. Grollier, Reservoir computing with the frequency, phase, and amplitude of spin-torque nanoscale oscillators, *Appl. Phys. Lett.* **114**, 012409 (2019).
- [25] S. Tsunegi, T. Taniguchi, K. Nakajima, S. Miwa, K. Yakushiji, A. Fukushima, S. Yuasa, and H. Kubota, Physical reservoir computing based on spin torque oscillator with forced synchronization, *Appl. Phys. Lett.* **114**, 164101 (2019).
- [26] T. Furuta, K. Fujii, K. Nakajima, S. Tsunegi, H. Kubota, Y. Suzuki, and S. Miwa, Macromagnetic Simulation for Reservoir Computing Utilizing Spin Dynamics in Magnetic Tunnel Junctions, *Phys. Rev. Appl.* **10**, 034063 (2018).
- [27] R. Nakane, G. Tanaka, and A. Hirose, Reservoir computing with spin waves excited in a garnet film, *IEEE Access* **6**, 4462 (2018).
- [28] T. Yamaguchi, N. Akashi, K. Nakajima, H. Kubota, S. Tsunegi, and T. Taniguchi, Reservoir computing with spin waves excited in a garnet film, *Sci. Rep.* **10**, 1 (2020).

- [29] D. Prychynenko, M. Sitte, K. Litzius, B. Krüger, G. Bourianoff, M. Kläui, J. Sinova, and K. Everschor-Sitte, Magnetic Skyrmion as a Nonlinear Resistive Element: A Potential Building Block for Reservoir Computing, *Phys. Rev. Appl.* **9**, 014034 (2018).
- [30] G. Bourianoff, D. Pinna, M. Sitte, and K. Everschor-Sitte, Potential implementation of reservoir computing models based on magnetic skyrmions, *AIP Adv.* **8**, 055602 (2018).
- [31] D. Pinna, G. Bourianoff, and K. Everschor-Sitte, Reservoir Computing with Random Skyrmion Textures, *Phys. Rev. Appl.* **14**, 054020 (2020).
- [32] W. Jiang, L. Chen, K. Zhou, L. Li, Q. Fu, Y. Du, and R. H. Liu, Physical reservoir computing using magnetic skyrmion memristor and spin torque nano-oscillator, *Appl. Phys. Lett.* **115**, 192403 (2019).
- [33] J. Grollier, D. Querlioz, and M. D. Stiles, Spintronic nanodevices for bioinspired computing, *Proc. IEEE* **104**, 2024 (2016).
- [34] X. Z. Yu, N. Kanazawa, Y. Onose, K. Kimoto, W. Z. Zhang, S. Ishiwata, Y. Matsui, and Y. Tokura, Near room-temperature formation of a skyrmion crystal in thin-films of the helimagnet FeGe, *Nat. Mater.* **10**, 106 (2011).
- [35] Y. Zhang, W. Zhao, J.-O. Klein, W. Kang, D. Querlioz, Y. Zhang, D. Ravelosona, and C. Chappert, in *2014 Design, Automation and Test in Europe Conference and Exhibition (IEEE, Dresden, 2014)*, Vol. 1, p. 1.
- [36] V. K. Joshi, Spintronics: A contemporary review of emerging electronics devices, *Eng. Sci. Technol. Int. J.* **19**, 1503 (2016).
- [37] C. Pfleiderer, Surfaces get hairy, *Nat. Phys.* **7**, 673 (2011).
- [38] N. Nagaosa and Y. Tokura, Topological properties and dynamics of magnetic skyrmions, *Nat. Nanotech.* **8**, 899 (2013).
- [39] A. Fert, V. Cros, and J. Sampaio, Skyrmions on the track, *Nat. Nanotech.* **8**, 152 (2013).
- [40] S. Seki and M. Mochizuki, *Skyrmions in Magnetic Materials* (Springer, Switzerland, 2015).
- [41] K. Everschor-Sitte, J. Masell, R. M. Reeve, and M. Kläui, Perspective: Magnetic skyrmions: Overview of recent progress in an active research field, *J. Appl. Phys.* **124**, 240901 (2018).
- [42] T. H. R. Skyrme, A non-linear field theory, *Proc. R. Soc. A* **260**, 127 (1961).
- [43] T. H. R. Skyrme, A unified field theory of mesons and baryons, *Nucl. Phys.* **31**, 556 (1962).
- [44] A. N. Bogdanov and D. A. Yablonskii, Thermodynamically stable “vortices” in magnetically ordered crystals. The mixed state of magnets, *Sov. Phys. JETP* **68**, 101 (1989).
- [45] A. Bogdanov and A. Hubert, Thermodynamically stable magnetic vortex states in magnetic crystals, *J. Mag. Mag. Mat.* **138**, 255 (1994).
- [46] U. K. Röbber, A. N. Bogdanov, and C. Pfleiderer, Spontaneous skyrmion ground states in magnetic metals, *Nature* **442**, 797 (2006).
- [47] S. Mühlbauer, B. Binz, F. Jonietz, C. Pfleiderer, A. Rosch, A. Neubauer, R. Georgii, and P. Böni, Skyrmion lattice in a chiral magnet, *Science* **323**, 915 (2009).
- [48] X. Z. Yu, Y. Onose, N. Kanazawa, J. H. Park, J. H. Han, Y. Matsui, N. Nagaosa, and Y. Tokura, Real-space observation of a two-dimensional skyrmion crystal, *Nature* **465**, 901 (2010).
- [49] H. B. Braun, Topological effects in nanomagnetism: From superparamagnetism to chiral quantum solitons, *Adv. Phys.* **61**, 1 (2012).
- [50] M. Mochizuki, Spin-Wave Modes and Their Intense Excitation Effects in Skyrmion Crystals, *Phys. Rev. Lett.* **108**, 017601 (2012).
- [51] M. Mochizuki and S. Seki, Dynamical magnetoelectric phenomena of multiferroic skyrmions, *J. Phys.: Cond. Matt.* **27**, 503001 (2015).
- [52] O. Petrova and O. Tchernyshyov, Spin waves in a skyrmion crystal, *Phys. Rev. B* **84**, 214433 (2011).
- [53] C. E. Zaspel, B. A. Ivanov, J. P. Park, and P. A. Crowell, Excitations in vortex-state permalloy dots, *Phys. Rev. B* **72**, 024427 (2005).
- [54] B. A. Ivanov and C. E. Zaspel, High Frequency Modes in Vortex-State Nanomagnets, *Phys. Rev. Lett.* **94**, 027205 (2005).
- [55] I. A. Surazhevsky, V. A. Demin, A. I. Ilyasova, A. V. Emelyanov, K. E. Nikiruy, V. V. Rylkov, S. A. Shchanikov, I. A. Bordanov, S. A. Gerasimova, D. V. Guseinov, N. V. Malekhonova, D. A. Pavlov, A. I. Belov, A. N. Mikhaylov, V. B. Kazantsev, D. Valenti, B. Spagnolo, and M. V. Kovalchuk, Noise-assisted persistence and recovery of memory state in a memristive spiking neuromorphic network, *Chaos Solitons Fractals* **146**, 110890 (2021).
- [56] Y. V. Ushakov, A. A. Dubkov, and B. Spagnolo, Spike train statistics for consonant and dissonant musical accords in a simple auditory sensory model, *Phys. Rev. E* **81**, 041911 (2010).
- [57] Y. V. Ushakov, A. A. Dubkov, and B. Spagnolo, Regularity of Spike Trains and Harmony Perception in a Model of the Auditory System, *Phys. Rev. Lett.* **107**, 108103 (2011).
- [58] O. Chichigina, D. Valenti, and B. Spagnolo, A simple noise model with memory for biological systems, *Fluct. Noise Lett.* **5**, L243 (2005).
- [59] B. Spagnolo, D. Valenti, C. Guarcello, A. Carollo, D. Persano Adorno, S. Spezia, N. Pizzolato, and B. Di Paola, Noise-induced effects in nonlinear relaxation of condensed matter systems, *Chaos Solitons Fractals* **81**, 412 (2015).
- [60] C. Guarcello, D. Valenti, and B. Spagnolo, Phase dynamics in graphene-based Josephson junctions in the presence of thermal and correlated fluctuations, *Phys. Rev. B* **92**, 174519 (2015).
- [61] C. Guarcello, D. Valenti, B. Spagnolo, V. Pierro, and G. Filatrella, Josephson-Based Threshold Detector for Lévy-Distributed Current Fluctuations, *Phys. Rev. Appl.* **11**, 044078 (2019).
- [62] C. Guarcello, D. Valenti, A. Carollo, and B. Spagnolo, Stabilization effects of dichotomous noise on the lifetime of the superconducting state in a long Josephson junction, *Entropy* **17**, 2862 (2015).
- [63] N. Bertschinger and T. Natschläger, Real-time computation at the edge of chaos in recurrent neural networks, *Neural Comput.* **16**, 1413 (2004).
- [64] R. V. Ababei, M. O. A. Ellis, I. T. Vidamour, D. S. Devadasan, D. A. Allwood, E. Vasilaki, and T. J. Hayward, Neuromorphic computation with a single magnetic domain wall, *Sci. Rep.* **11**, 15587 (2021).

- [65] K. Fujii and K. Nakajima, Harnessing Disordered-Ensemble Quantum Dynamics for Machine Learning, *Phys. Rev. Appl.* **8**, 024030 (2017).
- [66] G. Strang, *Introduction to Linear Algebra* (Wellesley-Cambridge Press, Wellesley, MA, 1993).
- [67] C. Schutte, J. Iwasaki, A. Rosch, and N. Nagaosa, Inertia, diffusion, and dynamics of a driven skyrmion, *Phys. Rev. B* **90**, 174434 (2014).
- [68] See, for example, Eq. (1) in D. Tan and Z. Chen, On a general formula of fourth order Runge-Kutta method, *J. Math. Sci. Math. Educ.* **7**, 1 (2012), or Eq. (8.17) in M. E. J. Newman, *Computational physics*, Seattle: Createspace (2013).
- [69] S. Seki, X. Z. Yu, S. Ishiwata, and Y. Tokura, Observation of skyrmions in a multiferroic material, *Science* **336**, 198 (2012).
- [70] A. Tonomura, X. Z. Yu, K. Yanagisawa, T. Matsuda, Y. Onose, N. Kanazawa, H. S. Park, and Y. Tokura, Real-space observation of skyrmion lattice in helimagnet MnSi thin samples, *Nano Lett.* **12**, 1673 (2012).
- [71] C. M. Bishop and N. M. Nasrabadi, *Pattern Recognition and Machine Learning* (Springer, New York, 2006).
- [72] H. Jaeger, Short term memory in echo state networks, GMD-Forschungszentrum Informationstechnik (2001).
- [73] J. Dambre, D. Verstraeten, B. Schrauwen, and S. Massar, Information processing capacity of dynamical systems, *Sci. Rep.* **2**, 514 (2012).
- [74] M. Inubushi and K. Yoshimura, Reservoir computing beyond memory-nonlinearity trade-off, *Sci. Rep.* **7**, 10199 (2017).

Correction: The previously published Figure 11(b) was processed improperly during the production cycle and has been fixed.